Nat. Hazards Earth Syst. Sci. Discuss., 2, 4525–4580, 2014
www.nat-hazards-earth-syst-sci-discuss.net/2/4525/2014/
doi:10.5194/nhessd-2-4525-2014

Natural Hazards and Earth System Sciences
Discussions
Open Access

Evaluating snow weak-layer rupture parameters through inverse Finite Element modeling of shaking-platform experiments

E. A. Podolskiy[1], **G. Chambon**[1], **M. Naaim**[1], **and J. Gaume**[2]

[1]IRSTEA (UR ETGR) – Centre de Grenoble, 2 rue de la Papeterie, BP 76, 38402 St.-Martin-d'Hères CEDEX, France
[2]WSL/SLF, Swiss Federal Institute of Snow and Avalanche Research, 7260 Davos Dorf, Switzerland

Received: 25 April 2014 – Accepted: 25 June 2014 – Published: 3 July 2014

Correspondence to: E. A. Podolskiy (evgeniy.podolskiy@gmail.com)

Published by Copernicus Publications on behalf of the European Geosciences Union.

Abstract

Snowpack weak layers may fail due to excess stresses of various natures, caused by snowfall, skiers, explosions or strong ground motion due to earthquakes, and lead to snow avalanches. This research presents a model describing the behavior of "sandwich" snow samples subjected to shaking. The Finite Element model treats weak layers as interfaces with variable constitutive behavior parameters. This approach is validated by reproducing cyclic loading snow fracture experiments. The model evaluation revealed that the Mohr–Coulomb failure criterion, governed by cohesion and friction angle, was adequate to describe the experiments. The "best fit" cohesion and friction angle were ≈ 1.6 kPa and 22.5–60°, indicating that the cohesion mainly determines the outcome of tests. The model showed complex, non-homogeneous stress evolution within snow samples and especially the significance of tension for fracture initiation at the edges of the weak layer, caused by dynamic stresses due to shaking. Accordingly, the previously used analytical solution, ignoring the inhomogeneity of tangential and normal stresses along the failure plane, may incorrectly estimate the shear strength of weak layers. The obtained parameters may constitute valuable elements in mechanical models used for avalanche forecasting.

1 Introductio

Dry snow avalanche release mechanics presents a key research question. Various mechanical models have been used to address the dry snow slab avalanche release problem focused on weak layer failure: e.g. crack models inspired by the over-consolidated clay theory (McClung, 1979), cellular-automata models (Fyffe and Zaiser, 2004), fiber-bundle model (Reiweger et al., 2009), physical-statistical models (Chiaia and Frigo, 2009), and multiple Finite Element Method, FEM (Stoffel, 2005; Podolskiy et al., 2013), analytical and empirical models (Zeidler and Jamieson, 2006). Recent studies, based on FEM with interfacial constitutive laws for weak layers, have shown that one of the

NHESSD
2, 4525–4580, 2014

key uncertainties in avalanche forecasting, spatial heterogeneity of weak layers, can be treated by statistical methods and that its importance is reduced for greater snow slab depths (Gaume, 2012; Gaume et al., 2012, 2013). Moreover, merging of FEM with terrestrial laser scanning input data (e.g. Teufelsbauer, 2009, 2011) and the growth of computer performance promise that this decade will see the possibility of precise estimation in terms of statistical distributions of potentially unstable snow masses for feeding into models of avalanche dynamics (Naaim et al., 2003). Accordingly, further investigation of the key research question about the weak layer mechanical behavior and constitutive law and their implementation by FEM are certainly needed for better quantitative understanding of the avalanche formation process.

For studying dry snow slab avalanches, various approaches have emerged and have been employed in FEM models to represent a snow weak layer under a cohesive slab; for detailed review refer to Podolskiy et al. (2013). Previous studies were mainly designed to investigate ~~the following:~~ (1) the stress state of a snow slab on a slope (Smith et al., 1972; Curtis and Smith, 1974; Smith and Curtis, 1975; McClung, 1979), (2) snow deformation (Lang and Sommerfeld, 1977), (3) skier loading (Schweizer, 1993; Wilson et al., 1999; Jones et al., 2006; Habermann et al., 2008; Mahajan et al., 2010), (4) weak layer heterogeneity, super weak zone length and stress concentration, as well as avalanche release slope angles (Bader and Salm, 1990; Stoffel, 2005; Stoffel and Bartelt, 2003; Gaume et al., 2011, 2012, 2013; Gaume, 2012), (5) fracture propagation properties (energy release or crack propagation velocity) (Mahajan and Senthil, 2004; Sigrist et al., 2006; Sigrist and Schweizer, 2007; Mahajan and Joshi, 2008), (6) coupled stress-energy model (Chiaia et al., 2008); anticrack energy release from slope-normal (vertical) collapse (Heierli et al., 2008), (7) structural size effect law (Bazant et al., 2003), (8) evaluation of field shear frame experiments (Jamieson and Johnston, 2001); and, finally, (9) snowpack response to explosive air blasts (Miller et al., 2011). To the best of our knowledge, no study has attempted to predict critical inertial loads for failure of ~~snow weak layers~~ in the case of cyclic loading, which

NHESSD
2, 4525–4580, 2014

presents a basis for model validation for an assessment of the effect of earthquakes on slope failure (Podolskiy et al., 2010a).

Previous FEM studies may be roughly classified into three principally different numerical approaches for consideration of weak layers: (1) a thin isotropic (or anisotropic) continuum (Bader and Salm, 1990; Jamieson and Johnston, 2001; Miller et al., 2011), (2) an interface with zero thickness and zero volume, which may be vertically "collapsible" or not (McClung, 1979; Stoffel and Bartelt, 2003; Gaume et al., 2012) or (3) a combination of the first two methods as a thin collapsible/non-collapsible layer with interfaces at the bottom and the top of it (Mahajan and Senthil, 2004; Mahajan and Joshi, 2008; Mahajan et al., 2010). The above-mentioned constitutive models and approaches are chosen based on the objectives of a study, and at the same time it may be noted that there is no universal, generally accepted framework for treatment of the "slab – weak layer" system. On the other hand, if we consider real weak layers, a few types can be distinguished in the field: non-persistent layers (precipitation crystals, or horizontally deposited plate-like snow crystals), persistent weak layers (buried surface hoar, depth hoar, faceted crystals and graupel) and different kinds of interfaces like ice lenses; sun, rain and wind crusts; or just interfaces between two layers of different densities (McClung and Schaerer, 2006; Föhn et al., 1998). Differences in fracture properties of each of these approximately ten types of layers are poorly understood (Föhn et al., 1998), and application of one particular approach from those listed above is unlikely to be physically relevant for all weak layer types (due to variable microstructural and fracture properties, thickness and residual friction of different types of crystals and interfaces). Moreover, due to the size of avalanche release zone, it is preferable to represent the weak layer by an interface, since its thickness is significantly smaller that the total snow height. By referring to volumetric layers, the FEM mesh size in the weak layer would have to be smaller than the size of crystals and thus may put the validity of the approach into question. More importantly, it is known from fracture line studies that poor bonding between layers may be a more significant cause of avalanching than low strength within weak layers (McClung and Schaerer, 2006). Accordingly, since the idea

NHESSD
2, 4525–4580, 2014

of treating weak layers as interfaces is attractive for large-scale applications (because of the discussion above), more studies are certainly needed.

2 Objectives and scope of the study

The aims of the present work are twofold. Firstly, we study the mechanical behavior of weak layers under accelerated cyclic loading in order to investigate the applicability of an assumed interfacial constitutive law to the analysis of previous experiments on failure of layered snow by Podolskiy et al. (2010b). Secondly, we analyse the experiments. These experiments were one of the first cold laboratory tests with snow "sandwich" samples, allowing study of the mechanics of weak layer dynamic failure. Complex variation of stresses and normal pressure in particular provided a unique dataset for investigating performance of the assumed failure law under highly variable conditions. In particular, as in Chiaia et al. (2008), we are interested to test the importance of including normal stress dependence in the failure criterion. We hypothesized and show that the well known Mohr–Coulomb failure criterion with cohesion, which includes normal pressure effects and tensile strength (one of the most common approaches in mechanics of granular materials), may be used as the first approximation to reproduce the dynamic experiments. Accordingly, an evaluation of the performance of this failure criterion as well as an evaluation of associated parameters (cohesion and angle of internal friction), through an analysis of tests and a comparison between analytical and FEM solutions, are the main objectives of the paper.

In snow science, the Mohr–Coulomb criterion is used, for example, for modeling snow erosion by flowing avalanches (Louge et al., 2011), for predicting critical inertial loads for failure of weak layers in seismically active regions (Matsushita et al., 2013; Pérez-Guillén et al., 2013), or for analyzing the packing of snow against sensor surfaces caused by wet avalanche (Baroudi et al., 2011). However, it is known that the rupture criterion alone is not sufficient for describing the full range of phenomena associated with snow weak layer failure or the release of snow slabs. It is one ingredient

NHESSD
2, 4525–4580, 2014

among others, needed for complete slab avalanche modeling (e.g. tensile slab failure, stauchwall effects, heterogeneity, post-peak softening, fracture propagation ~~or possible~~ normal collapse; Heierli et al., 2008).

For the scale of our tests, which are not focused on the process of fracture propagation starting from weak zones or imperfections and leading to avalanche release, self-propagating crack is not directly relevant. This is so because our experiments, similarly to work by Reiweger and Schweizer (2010), are related to failure initiation and larger field experiments are needed to study fracture propagation (and due to other reasons further explained below). Also, for the small scale of our case, the crack propagation is not relevant because the critical size of the weakness is known to be larger than our samples (McClung, 2011b). Furthermore, the rate of high-speed video records taken during the experiments (i.e. frequency 250 Hz; Podolskiy et al., 2010b) did not allow us to investigate the fracture propagation process in detail. However, we note that the crack always occurred between two consecutive video frames (thus it did not last longer than 4 ms). A study of crack propagation, a topic that has received a lot of attention recently (Birkeland et al., 2009), at such speeds should be based on computationally costly dynamic fracture mechanics, and is beyond the focus and scope of the present experiments and the paper.

In the present work we consider a weak layer as an interface. The experiments referred to in this paper are well suited for this objective and the context. We remain mindful that our simple approach, including an interface with Mohr–Coulomb failure criterion, may serve as suitable and computationally effective basis for the ultimate purpose of upscaling the method for large-scale simulations. For example, every dynamic snow avalanche simulation starts with the prescription of avalanche release height and volume. Together with entrainment of new snow down-slope these initial conditions strongly determine the outcome of modeling in terms of run-out distance and impact pressures.

To that end, this paper is organized according to the following structure. Sections 3.1–3.2 explain methods of previous cold laboratory experiments performed by

NHESSD
2, 4525–4580, 2014

(Podolskiy et al., 2010b) and Sect. 3.3 presents some background about the Mohr–Coulomb criterion. Section 4 introduces the methods of this paper: 2-D model, including the details of weak layer representation adapted for our FEM analysis. It also describes a simulation of accelerated cyclic loading on a 2-D sample and the procedure of numerical optimization. Finally, Sects. 5, 6 and 7 present the obtained results, sensitivity tests, discussion and conclusions.

3 Experimental and theoretical background

3.1 Shaking platform experiments

The paper take into account a series of snow samples which were tested using the shaking platform described by Nakamura et al. (2010) and Podolskiy et al. (2010b). The procedure could be briefly summarized as follows: samples were frozen to the platform and loaded via inertia due to initiation of the platform's horizontal oscillations from right to left with limited amplitude, but with growing frequency of oscillations. The latter caused increases in velocity, acceleration, and thus stresses within the samples; at the point when the increasing stress exceeded the strength of snow the sample failed. High-speed video records, accelerometers and measurement of the fractured mass revealed the instant of failure and the corresponding peak acceleration (Nakamura et al., 2010; Podolskiy et al., 2010b). Originally, this dynamic experimental approach was developed for studying the shear strength properties of snow and their relationship to vibrations (Abe and Nakamura, 2000, 2005; Nakamura et al., 2000a, b, 2010). These previously reported tests were performed on homogeneous blocks of snow. Due to this snow structure and configuration, cracks could not be localized in one 2-D failure plane and had complex 3-D geometries that were different from case to case, thus inhibiting straightforward interpretations. Podolskiy et al. (2010b) introduced a weak layer into the blocks and the possibility to incline the platform; these two points make the study more relevant to dry snow slab avalanche release. Nevertheless, free surfaces on five sides

NHESSD
2, 4525–4580, 2014

of the sample and the probability of edge effects in response of a snow block to loading restrict the possibility of simple stress assessments and relating the experimental results to a real snowpack at slope scales. The question of a normal stress effect on the failure of weak layers during experiments is particularly interesting. Without FEM analysis it is hard to estimate its non-homogeneous spatial and temporal evolution within the sample (the same should be noted about shear stresses). For example, an attempt by Nakamura et al. (2010) to calculate dependence of shear strength on presumably constant overburden pressure produced surprisingly high values of internal friction angle (73.4–83.1°) with zero cohesion, thus exemplifying the importance of understanding normal stress oscillations in the experiments for reliable interpretations.

The experiments, reproduced in this study, were performed in a cold laboratory (with an ambient air temperature of −10 °C) on artificial "sandwich" snow samples (two blocks of snow with a weak layer made of low density snow placed approximately at mid height). In total, 19 individual tests with varying properties were modeled. Most relevant parameters and results of experiments are indicated in Table 1; for more details refer to Podolskiy et al. (2010b). The samples were prepared by sieving artificial precipitation snow over a cohesive slab, covering it with another slab, and later cutting vertically the resulting structure into smaller blocks. The resulting weak layer density was around 100 kg m^{-3}, and its thickness was around 1–2 cm. If we attempt to identify the closest type of natural weak layer to the artificially created horizons in the middle of snow samples, it would be a non-persistent precipitation layer, made of low density, partly decomposed dendrite crystals, or DFdc according to classification by Fierz et al. (2009). The length, width and height of specimens were 0.3, 0.2, and 0.2–0.45 m, respectively. The masses overlaying the weak layers ranged between 1.3 and 4.6 kg. This difference in mass was created by varying the height of the upper block by the additional snow frozen immediately before each test to create larger normal pressures. The samples, once frozen to the platform, were vibrated by shaking-platform horizontal oscillations with an amplitude of 1.65 cm until fracture along the weak layer. The latter was documented with high-speed video camera. Additionally, by varying inclination of the

NHESSD
2, 4525–4580, 2014

platform we produced tests with several slope angles (0, 25 and 35°). For these inclined tests geometry of the sample side cuts was always kept vertical. The critical peak accelerations (in the range of 2.23–6.36 g) corresponding to failure of the samples were recorded during each experiment by a horizontally installed acceleration transducer and were used for estimation of shear strength values of the weak layer (as discussed later). From the different types of tests performed by Podolskiy et al. (2010b), we select only the weak layer fracture tests made with horizontal single-degree-of-freedom oscillations (at the same time we emphasize that a sample may have various inclinations: 0, 25 or 35°).

3.2 Some further experimental conditions relevant to construction of the model

In the majority of experiments weak layer fractures were observed at the lower interface (between the weak layer – and the lower block). No vertical collapse within the weak layer could be recognized during tests (based on video quality we could only restrict the maximum possible collapse as less than 1 mm). Moreover, due to the absence of a crystalline structure that could be associated with any significant volumetric collapse, we do not expect to have it on a large scale (for example, an order of 3–40 mm was documented by van Herwijnen et al., 2010; van Herwijnen and Jamieson, 2005).

Furthermore, we omit the bottom block from modeling in order to reduce computational time based on the following logic. The lower block can be considered as a rigid base of the interface and moves together with the boundary, the overall mechanical behavior of the system may be reproduced by only the upper block and the interface (Fig. 1). This statement can be supported by observational constraints for shear strains made during the experiments before failures. Analysis of video records shows no noticeable horizontal strains in the blocks; due to limitations of the video quality, the maximum estimate for strain is less than 0.33 %. This means that the whole block is a rigid oscillator, thus allowing us to omit the lower block. Moreover, such assumption is valid considering the fact that most of the possible deformation is concentrated within the

NHESSD
2, 4525–4580, 2014

weak layer (e.g. loading experiments by Reiweger and Schweizer, 2010 reported that 90 % of the sample's global deformation was concentrated in the weak layer).

These facts allow simplification of the model assumptions and remove the necessity of considering vertical collapse, which is still an argued question in the literature (e.g. Birkeland et al., 2009; McClung, 2011a; McClung and Borstad, 2012), and the lower block. Thus, for the sake of simplicity, we reduce our problem to a single block with an interface at its lower part and boundary conditions.

Since the experiments had high rates of loading to failure (within a second; strain rates were higher than 10^{-3} s^{-1}), we do not refer to viscous behavior and assume a purely elastic constitutive model for snow. High loading rates guarantee a brittle range for all observed fractures. Such high rate loadings, discussed in this paper, are relevant for any brittle fractures in snow, which can be induced due to natural releases, loading produced by skiers/snowmobilers, explosive air blasts, as well as strong ground motion due to earthquakes or mine blasting (Podolskiy et al., 2010a).

3.3 Mohr–Coulomb failure criterion for snow and scope of this study

The idea of describing the failure of snow according to the Mohr–Coulomb failure criterion has been an attractive idea for some purposes since Haefeli (1963), Roch (1966), Mellor (1975), and has been used recently (Vidal, 2001; Louge et al., 2011; Matsushita et al., 2012). According to Mellor's review (Mellor, 1975) cohesion can be associated with time-dependent intercrystalline bonding (sintering) while the angle of internal friction can be imagined as initial or residual strength of snow with broken bonds.

Many experimental studies investigated the effects of normal load on shear strength of snow and snow weak layers, mainly through shear frame or shear vane tests. Experiments, showing an influence of normal stress on various snow types, were performed by Roch (1966), DeMontmollin (1978, 1982), McClung (1977), Perla and Beck (1983) and Navarre et al. (1992). Jamieson and Johnston (1998) reported similar influence on non-persistent weak layers, but found no significant effect on persistent weak layers, thus proposing $\phi = 0^{\circ}$. Mellor (1975) suggested the idea of using Mohr–Coulomb

NHESSD
2, 4525–4580, 2014

failure criterion could be problematic, for example, due to changes of the state of the material under pressure (which also depends on temperature). Recently Matsushita et al. (2012) made tests with artificial precipitation snow to investigate temporal variation of the shear strength and concluded that the influence of normal load on the strength was more significant than temperature. Overall, most studies investigated the influence of normal pressure using shear-frames, while results obtained with alternative methods, like shaking platform tests (Nakamura et al., 2010; Podolskiy et al., 2010b), may also provide new valuable insights and thus remain to be understood.

The experiments shown here suppose that no changes in cohesion had taken place during experiments, since no significant changes of vertical dimensions of samples before and after failure could be observed, and thus provide an opportunity to explore the applicability of the Mohr–Coulomb criterion to some degree. High-speed video analysis of extended column tests by van Herwijnen and Birkeland (2014), which involve repeated tapping on a snow column containing a weak layer, indirectly support this assumption (they confirmed that no accumulation of damage could be seen within the weak layer, similarly to the experiments discussed here).

Furthermore, considering micro-scale, McClung and Schaerer (2006) noted that the "formation of snow avalanches and the origin of fractures begins at a scale which is at least 100 times the grain size within the weak layer so that individual grain bonds don't matter much even if they could be properly dealt with". For the sake of simplicity we neglect bond-scale processes responsible for development of micro-flaws as well as fatigue. The latter may be refuted as a possible alternative explanation of the experimental results due to no observations indicating that samples subjected to oscillations of longer duration failed at lower accelerations (Podolskiy et al., 2010b).

Accordingly, the experiments presented here are above the micro-scale, but below the avalanche release scale, and allow to focus only on the failure criterion of snow (i.e. strength). In this light, progressive failure in this study will be driven only by inertial loading (due to oscillations of the shaking platform). Thus we are testing the Mohr–Coulomb failure envelope, which plays a role of failure threshold, and do not investigate

NHESSD
2, 4525–4580, 2014

post failure phase. We are mindful that in follow-up studies the criterion could be complemented or refined by other effects, like post-peak softening (Gaume et al., 2013) for larger scales.

4 Methods

4.1 FEM model

We perform FEM analysis using Cast3M software (http://www-cast3m.cea.fr), a code developed by the French Atomic Research Center (Laborderie and Jeanvoine, 1994), and employed in previous studies on snow avalanche release (Gaume et al., 2011, 2012, 2013; Gaume, 2012). The code (Education and Research Release, 2010) employs an implicit time integration scheme; governing equations are solved incrementally thus enabling non-linear computations and taking into account dynamic effects. In regard to the differences with other available programs (Podolskiy et al., 2013), we note that Cast3M is open-source software, which allows modifications to be made to the source code.

4.2 Model description

4.2.1 Model geometry

In order to reproduce the geometry and parameters of the experiments (Podolskiy et al., 2010b), the initial 2-D geometry for a slab is presented by a rectangle or parallelogram (for inclined tests), which is 0.3 m long and 0.14–0.36 m high. A quadrilateral element shape with four nodes is used for the mesh (QUA4); there are about 14–36 elements in the vertical dimension (depending on the sample height) and 30 in the horizontal dimension (1 cm by 1 cm each). The chosen mesh shape is the most common type of mesh used by previous FEM studies on snow (Podolskiy et al., 2013), especially since we deal with non-curved geometry and no large strains. We note, that sensitivity tests

NHESSD
2, 4525–4580, 2014

with twice higher number of elements produced similar, but much more computationally costly results.

For representing the weak layer of the "sandwich" samples we treat it as an interface. The interface is modeled by joint elements with four nodes (JOI2) but zero thickness, i.e. an element is created between two segments of two points (Fig. 1c). There are 30 elements (each 1 cm long). The "lower" part of the joint (${}_1A'-{}_2B'$; Fig. 1c) is fixed to the bottom boundary, meaning that vertical and horizontal displacements of this part of the joint are forbidden relative to the boundary. However, the lateral and surface boundaries of the rest of the system are not restricted, thus allowing free deformation. Therefore, these conditions are both comparable to those of a snow block frozen to the platform.

We note that the simulated geometry requires half as much computational time as it do if the lower block is included. Furthermore, as it will be shown (Sects. 4.2.2 and 4.2.5), by introducing interface stiffness (which may be seen as equivalent to putting the sample on an elastic cushion instead of a rigid plate) and making sensitivity to a wide range of values, it is possible to verify if our assumption is reasonable. The stiffness was found as not playing any important role in the key quantities controlling interface failure process (Sect. 5.3). In view of this simple observation it is quite obvious that the assumed model geometry does not control failure.

4.2.2 Constitutive laws of the block and the interface

The upper block is considered as a uniform and isotropic elastic material similarly to many slab models presented in literature (Mahajan et al., 2010; Heierli et al., 2008; Bazant et al., 2003; Borstad and McClung, 2011). Accordingly, its behavior is controlled by Young's modulus, E, and Poisson ratio, υ. Also we note that since the problem deals with dynamics and vibration, non-physical viscosity of the block, η, is introduced into the damping matrix of the model for numerical stability reasons. A choice of material properties of the block (i.e. Young's modulus, Poisson ratio) will be considered below

NHESSD
2, 4525–4580, 2014

(Sect. 4.2.5). Sensitivity tests to Young's modulus, E, Poisson ratio, υ, and viscosity, η, will be shown in Sect. 5.3.

The assumed behavior of the interface is that of a joint model based on the Mohr–Coulomb failure criterion, which is controlled by the angle of internal friction, ϕ, and cohesion, c:

$$\tau = \sigma \tan(\phi) + c, \tag{1}$$

where τ is shear stress and σ is normal stress (Fig. 1d). The cohesion is defined in the model through the tensile strength, σ_{st}, as follows:

$$c = \sigma_{st} \tan(\phi). \tag{2}$$

Accordingly, we may refer in the following text to both of them (tensile strength, σ_{st}, and cohesion, c) depending on the context. Such substitution implies that the failure envelope, having a slope equal to the angle of internal friction, ϕ, intercepts the shear axis at c, and the normal stress axis at σ_{st} (Fig. 1d). This constitutive relationship was chosen because interfaces without any tensile strength would not be adequate for reproducing the tests, which may have significant tension stresses (as it will be illustrated later). Additionally to failure criterion, for joint elements we specify values of shear and normal stiffness, K_s and K_n, which control strains of the interface (more details are provided in Sect. 4.2.5).

4.2.3 Definition of interface failure

We define the occurrence of total sample failure as the first instant when all nodes of the interface, N, satisfy the Mohr–Coulomb failure criterion:

$$[\text{nodal failure}] \equiv \frac{|\tau| - \sigma \tan\phi}{c} = 0.99999, \tag{3}$$

$$[\text{total failure}] \equiv N_f = N, \tag{4}$$

NHESSD
2, 4525–4580, 2014

where N_f is a number of failed nodes. The instant when this condition is satisfied ($N_f = N$) is treated as the moment of total sample failure, t_m. We just note that for prescribed c and ϕ, and for dynamically changing shear and normal stresses, τ and σ, Eq. (3) simply corresponds to the failure criterion (Eq. 1) rewritten in a form that allows identification of when it is satisfied within the model. ~~Against the above mentioned background and the size of specimens (Sect. 3.3), the implemented approach~~ means that a local node meeting the criterion leaves the system unchanged (i.e. there is no loss of strength leading to a non-linear behaviour), and that system failure can only occur if all interface nodes simultaneously satisfy the failure criterion.

4.2.4 Cyclic displacements, inertial loadings and gravity

Before the simulation of inertial loading can be initiated for a particular set of parameters, first, we subject our domain to its actual weight. For this the matrix of mass is multiplied by a field of gravitational acceleration in the vertical direction. Here, the gravity is applied (to nodes) gradually (i.e. 2.45 g s^{-1}) until reaching its 100 % value within the first phase of simulation, in order to avoid any possible vibration of stresses (within the first 4 s followed by another 0.4 s for stabilization of the system). Initially the gravity is imposed on a material model with a Poisson ratio, υ, of zero, for obtaining homogeneous normal stresses within the sample, i.e. without any stress concentrations at the edges. In the next procedural step the material model is replaced by a model with a new Poisson's ratio $\upsilon = 0.04$ (more details are shown in the next Sect. 4.2.5).

Next, we reproduce horizontal shaking of the platform and, accordingly, introduce inertial forces within the sample by imposing displacements onto the boundary. To recreate the dynamics of our experimental problem we define cyclic basal displacements in the model with an amplitude similar to the one produced by the motor during experiments. Thus, the block moves horizontally a distance $s(t)$ according to the following trajectory:

NHESSD
2, 4525–4580, 2014

$$s(t) = 0.0165(1 - \cos(\omega(t)t)), \tag{5}$$

where 0.0165 is a displacement amplitude in meters (it corresponds to the amplitude of horizontal oscillation of the shaking platform used in experiments). The angular frequency coefficient, ω, starts to evolve after the initial preparation of the sample (described earlier) and increases linearly as a function of time:

$$\omega(t) = \begin{cases} 0 & \text{if } 0 < t < 4.4\,\text{s}, \\ k_\omega \pi(t - 4.4) & \text{if } 4.4 \le t \le 25.0\,\text{s}. \end{cases} \tag{6}$$

This angular frequency, controlled by the coefficient k_ω (varying between 0.44 and $1.43\,\text{s}^{-2}$ and explained further below), introduces the gradual growth of velocities and accelerations, and thus, stresses, with every oscillation (Fig. 2). Accordingly, almost all stresses in our system (except gravitational) are driven solely by the horizontal oscillations of the boundary.

Here, it is also appropriate to provide a simplified analytical evaluation of the shear force evolution (τ_{ex}) used to estimate weak layer shear strength during experiments (Nakamura et al., 2010; Podolskiy et al., 2010b) in order to see differences with the FEM solution:

$$\tau_{ex}(t) = \frac{m_f a(t)}{A}, \tag{7}$$

where m_f is a mass of the upper block and A is the area of the failure plane. This analytical solution could also be called a static model, since it does not account for dynamic stress inhomogeneities caused by inertia and geometry. Since our simulation is in 2-D and since $m_f = h_s A \rho_s$, where h_s is the height of the block and ρ_s is its density, Eq. (7) can be rewritten for feeding simulation data into it and for further comparisons as (horizontal case):

$$\tau_{ex}(t) = h_s \rho_s a(t). \tag{8}$$

NHESSD
2, 4525–4580, 2014

Similarly, the inclined case may be expressed as:

$$\tau_{ex}(t) = h_s \rho_s a(t) \cos\alpha + h_s \rho_s g \sin\alpha, \quad (9)$$

where α is the inclination of the boundary and the right term corresponds to shear stress due to gravity.

4.2.5 Choice of constitutive parameters

Young's modulus

For experimental snow densities of upper blocks (212–226 kg m^{-3}), corresponding values of Young's modulus, E, vary depending on the literature source (e.g. Mellor, 1975; Stoffel, 2005; Habermann et al., 2008). For simulating upper blocks we use modulus values as a function of density after Mellor (1975) of 1.2–1.5 MPa.

In regard to the high strain-rates of the experiments considered here (10^{-3}–10^{-1} s^{-1} for the block Nakamura et al., 2010, 2012), we should note that there is one possible effect of the rate on the elastic properties of snow. A possible increase of Young's modulus with higher strain-rates was estimated to correspond up to a factor of 3 (e.g. Kry, 1968). For our tests this illustrates that the order of magnitude of E remains the same and our assumptions are still consistent with Mellor's review (which provides the most comprehensive summary of static and dynamic E and has not been improved much by any recent studies; for more examples see Nakaya, 1961; Shapiro et al., 1997; Podolskiy et al., 2013). Furthermore, for similarly high strain rates, Jamieson and Johnston (2001) as well as Nakamura et al. (2010) used values of Young's modulus after Mellor (1975) as a function of density. Therefore, there are no strong limitations to following them and using the modulus from Mellor's paper for the purposes of the present study. Sensitivity tests for higher Young's Modulus, E, are presented in Sect. 5.3. However, we note that the block is a quasi-rigid object and higher values of the modulus are not expected to produce significant changes in the model.

NHESSD
2, 4525–4580, 2014

Poisson ratio

For a comparable range of densities, Poisson's ratio of snow, υ, is usually chosen in other FEM studies to be around 0.25–0.3 and thus corresponds to Poisson solid (McClung, 1979; Jamieson and Johnston, 2001; Habermann et al., 2008; Borstad and McClung, 2011). However, considering experimental studies (Gubler, 1994; Salm, 1971; Ooizumi and Huzioka, 1982), a speculative Mellor's envelope for the Poisson's ratio as a function of density (Mellor, 1975) and the most recent effort by Teufelsbauer (2011) to refine the Poisson's ratio (which he calls viscous, as a function of density and temperature), we follow the latter study and select a Poisson's ratio for the block to be equal to 0.04 (for temperature –10 °C and density 212 kg m^{-3}). Furthermore, the Teufelsbauer approximation covers the comparable range of values of those appearing in reviews on snow slab avalanches (e.g. Schweizer, 1999), and in high strain-rate measurements (Ooizumi and Huzioka, 1982). Thus the chosen value is consistent with available experimental data. However, sensitivity tests with a higher value of this parameter (0.23) showed that it is not important for the failure results (see Sect. 5.3).

Shear and normal stiffness of the interface

Shear and normal stiffness, K_s and K_n, control the resistance of the joint to vertical and horizontal deformations in response to an applied load. Usually assumed shear stiffness is taken as being equal to a half of normal; moreover, anisotropic layers of buried surface hoar were shown to be softer in shear than in compression (Jamieson and Schweizer, 2000). Nevertheless, to the best of our knowledge, there are no reliable experimental data for weak layer elastic properties. After conducting sensitivity tests for different couples of K_s and K_n (within the range 10^5–10^8 N m^{-3}) for a full set of experiments, the shear and normal interface stiffnesses were set to 10^8 N m^{-3} to reduce peak elastic displacements of the whole system to realistic values on the order of 10^{-3} m. Some studies assume smaller values, e.g. 10^{-4} m in weak layers, but note that such precise measurements are not available for alpine snow (McClung, 2011a).

NHESSD
2, 4525–4580, 2014

In our case we take it as simply an experimentally verified fact, and note that even if an order of magnitude reduction of stiffness (to 10^7 or $10^6\,\mathrm{N\,m^{-3}}$) resulted in larger displacements ($\sim 10^{-2}$ m or higher), no difference in terms of failure was observed. We notice that different shear and normal stiffness values, e.g. 5×10^7 and $10^8\,\mathrm{N\,m^{-3}}$ respectively, gave same results in terms of failure as when K_s was set equal to K_n.

For comparison with other studies we may find an equivalent value of Young's modulus for the stiffness values considered in numerical optimization of our study (Sect. 4.4). Such equivalent is defined as $E_{wl} = K_{s,n} h_w$, where h_w is the typical thickness of the weak layer. For example, stiffness values 5×10^7 and $10^8\,\mathrm{N\,m^{-3}}$ are equivalent to Young's modulus 0.5 and 1 MPa. We also note that the similar and even higher magnitudes of Young's modulus equivalents to those used in our study were employed for modeling snow weak layers in other FEM studies (Mahajan and Senthil, 2004; Sigrist et al., 2006; Mahajan and Joshi, 2008). Sensitivity tests with lower stiffness, for example, equivalent to a softer Young's modulus of 0.1 MPa, correspond to larger interface horizontal displacements at peak stresses, like 0.5 cm, and thus are considered unrealistically high. More importantly, we found negligible effects of K_s and K_n on failure as it will be discussed later in Sect. 5.3.

4.3 Computational approach

A few other issues exist that require additional consideration: (1) the masses of the snow blocks above the weak layers were different from one case to another (and thus, also the sample height), (2) the angular frequency increment was not constant for all experiments due to manual control of its rate. Accordingly, this means that for our FE model the former and the latter factors require individual selection of the height (h_s), as well as an appropriate rate for frequency growth (k_ω), respectively.

First, we prescribe to each sample an h_s – equivalent derived from the recorded mass and density (such that $h_s = m_f/(A\rho_s)$; Table 1). Next, since any sample's failure occurs at an instant when a particular critical acceleration reaches a peak (caused by

NHESSD
2, 4525–4580, 2014

a change of the platform's direction of movement), and since the moment of failure and the corresponding peak acceleration are known from measurements, we individually adjust the coefficient k_{ω} for each test so that the instant of the observed failure (t_e) is reached at the right value of the peak acceleration. The latter allows us to achieve similar acceleration conditions of the model to those of the experiment at the instant of failure, t_e. In order to reach the measured peak accelerations, k_{ω} should vary between 0.44 and 1.43 s^{-2} (Fig. 3). An example of k_{ω} adjustment for one test is provided in Fig. 3a and b. The experimental range for accelerations and time of fracture (t_e), where modeling results should fall into, is shown in Table 1. Values of k_{ω} and material/mechanical properties are listed in Table 1 and 2.

Finally, by adjusting the two remaining degrees-of-freedom (c and $\tan\phi$) we investigate the ability of the assumed constitutive law to predict failure time, t_e. Accordingly, fitting values of cohesion and angle of internal friction, c and ϕ, is the main objective of the study. If the law is valid and may reproduce the variety of presented conditions, we expect to obtain a pair of c and ϕ valid for all the tests, since all experimental procedures were aimed at producing similar weak layer properties, which were made of the same snow type. The underlying numerical procedure is described below. After computations, we also compare the analytically obtained stresses (Eqs. 8 and 9) with those from the FE analysis.

4.4 Search for optimal failure parameters

We assume that for a given set of prescribed parameters (i.e. given material and mechanical properties) and experimental criteria (e.g. acceleration at failur the best to reproduce the experiments). Our goal is to find a set of c and ϕ that minimizes the time difference between the model predicted failure (t_m) and the test failure (t_e), i.e. $|t_m - t_e|$ for all tests. We consider a parameter space where cohesion, c, is limited to a range between 0.5 and 2.8 kPa (Föhn et al., 1998), and the internal friction coefficient range is to 0.18–3.73, or 10–75° (e.g. Keeler and Weeks, 1968; Nakamura et al., 2010); more detailed discussion is provided in Sect. 6. Accordingly, to move through our parameter

NHESSD
2, 4525–4580, 2014

space, we chose a numerical optimization search procedure based on the following constrained single-objective cost function, C_{FEM}:

$$C_{\mathrm{FEM}}(c,\phi) = \sqrt{\frac{\sum_{i=1}^{n} |t_{\mathrm{m}i} - t_{\mathrm{e}i}|}{n}} \tag{10}$$

for a number of simulated tests n. C_{FEM} is basically the Root Mean Square Error (or RMSE).

Numerical optimization is performed for the whole set of simulations (or for the sample set, as discussed below); for minimizing the $|t_{\mathrm{m}} - t_{\mathrm{e}}|$, we repeat FE simulation with adjusted input parameters.

In order to reduce computational costs, instead of covering our c–ϕ parameter space by all possible discrete combinations, after the first simulations introduced the overall response of the whole ensemble of tests (19 in total) to seven different parametric set-ups (combinations of fixed values of c and ϕ, K_{s} and K_{n}) and the identification of possible outliers, we followed cost function gradients manually by selecting a small representative sample of experiments for calibration. Thus we reduced the total population of tests to a representative "calibration" sample, consisting of 5 (or 9) individual tests (selected with varying inclinations, masses and sizes to avoid possible biases). The results obtained with the "calibration" sample, in their turn, will be verified by using the same parameters for the "validation" sample (as will be explained in Sect. 5.2). It is important to note that such a validation procedure allows confirmation that the optimal parameters also work for other tests. Thus, a segregation of tests into "calibration" and "validation" samples presents an additional way to verify the results.

NHESSD
2, 4525–4580, 2014

5 Results

5.1 Mechanical behavior of samples and failure

~~For realistic values of Young's modulus assumed in the model, FEM results support the argument of Sect. 3.2 saying that the block is a stiff oscillator.~~ Figure 4 provides examples of stress inhomogeneities within the blocks caused by motion and the geometry of the system. In this regard, two principal observations may be made for all types of inclinations. ~~(i)~~ First, as the block changes its direction of movement and thus experiences high accelerations, we observe the expected emergence of maximum shear stress (see instant t_2 at Fig. 4). These stresses decay as the block moves backward and passes through the central position of its trajectory (t_3). At the opposite side of the oscillation (t_4) shear stresses re-emerge with higher amplitude and opposite sign (Fig. 4). ~~(ii)~~ Second, we see that at the critical points (t_2 and t_4), normal stress remains quasi-constant in the middle of the block, but may have opposite signs at the edges. Meaning that due to the inertia of the mass (which is fixed to the boundary), one side will ~~have~~ an increase ~~of~~ normal stress, while the other a decrease. With higher accelerations, these decreasing normal stresses may turn into tension. As the block leaves the point t_2 and reaches the opposite critical point (t_4), signs of normal pressure ~~flip~~.

Similarly, in the interface the imposed oscillations gave shear stresses with changing directions and produced strong oscillations of normal stress at the edges of the joint (Figs. 5 and 6). Tensile stresses appearing at the edges of the joint after the start of oscillations clearly illustrate that tensile strength of the weak layer needs to be taken into account for realistic representation of tests (Fig. 5). Figure 6 shows the differences between the analytical (Eqs. 8 and 9) and FEM solutions for shear stresses. For example, for the assumed parameters the FEM gives larger shear stresses (by about 20 % in the middle of the horizontally inclined joint). For the inclined tests (25 and 35°), the differences between the analytically and FE in the middle of the interface derived shear stresses are slightly smaller (Fig. 6b and c). However, edge effects are more significant

NHESSD
2, 4525–4580, 2014

for these inclined tests (Figs. 5 and 6) due to geometrical effects, thus clearly indicating limitations of the analytical approach (Eq. 7) for samples of limited length.

Figure 7 shows the growth of the number of nodes, N_f, that had reached failure criterion with time. Here we note that the propagation of the failure condition is not self-induced, but is a load driven process. And as stresses are removed, there is no flaw remaining. As the block passes the critical point of its trajectory (where it has a full stop and thus experiences the highest accelerations) and reverses its direction (Fig. 7), the stresses start dropping so that no nodes remain under failure ($N_f = 0$). The next peak is larger than the previous one because at the next oscillation the accelerations are larger by some increment, as are the stresses (meaning that with each oscillation we produce a larger loading with higher magnitude), and thus more nodes satisfy the failure criterion. Thus there is no cumulative accumulation of failed nodes. Accordingly, we observe progressive enlargement of the failure zone with higher stresses (Fig. 7), but not crack propagation, therefore we could call it a numerical indication about how close the system is to failure.

~~By definition in our model the failure is the first instant when the interface experience stresses which none of its nodes is able to sustain.~~ The time difference between the instant of "total failure" (t_m) and experimental failure (t_e) is also indicated ~~at~~ Fig. 7. ~~The behavior of this difference and the process of reducing it is discussed below for all experiments.~~

5.2 Mohr–Coulomb parameter optimization

The overall response of all tests to various parameters is provided in Fig. 8. For the considered range of parameters ~~(see Sect. 4.4 and the figure's legend)~~, time-to-failure, t_e, is reproduced within ±2.5 s accuracy for the majority of tests with only a few outliers larger than that. This figure shows that, for example, if the modeled joint has a cohesion that is too high, failure will be delayed compared to t_e; on the contrary, if it is too low, failure will occur earlier ~~than the observed one (Fig. 8).~~ In this light, the responses of individual tests look similar for all tests with the same parameters, suggesting that

NHESSD
2, 4525–4580, 2014

instead of using all of them, we may select a smaller sample for calibration of cohesion c and angle of internal friction ϕ.

Figure 9 shows cost function, C_{FEM}, sensitivity to a selection of a different number of tests and illustrates that such "downscaling" is reasonable and efficient for the optimal parameter search. This is true because for particular variations in parameters a sample's C_{FEM5} (where subscript 5 indicates a number of tests) responds similarly to C_{FEM} computed for the complete population of tests. Later, in order to check C_{FEM} sensitivity to number of tests taken into account, results obtained with the "calibration" sample (tests: 27, 30, 33, 35, 41) were verified with a larger number of tests. And in addition the results were also verified with another "validation" sample, presented by the remaining tests (shown below).

The evolution of the sample's C_{FEM} with the prescribed cohesion and angle of internal friction, c and ϕ, is shown in Fig. 10 (and in Table 3). The figure shows all tested combinations of c and ϕ together with some sensitivity tests. All exact values are provided in Table 3. The most important feature of the parameter optimization (Fig. 10) is a lack of one clear global minima. In Fig. 10 this tendency is expressed as an area, which is narrow in cohesion c, but wide in ϕ, and which has very close values of C_{FEM} (this is more clearly seen in the color contours based on a cubic interpolation). Accordingly, it is evident that simulation results are more sensitive to the cohesion than to the angle of friction. ~~A more detailed interpretation of the significance of this region in terms of the Mohr–Coulomb failure envelope will follow in the discussion Sect. 6, together with comparison to other studies~~.

Following the finding that some simulations with different pairs of $c - \phi$ resulted in comparable values of cost function C_{FEM} (Table 3), we attempted to increase the total number of tests in the sample for each of these runs with low C_{FEM} from 5 individual tests to 9 (include tests: 23, 26, 32, 39). However, even with additional tests (Fig. 10; Table 3) a minimum did not become evident. We found three pairs (1.57 kPa – 30°, 1.57 kPa – 35°, 1.6 kPa – 30°) that may represent the minimum (C_{FEM9} = 0.365 s,

NHESSD
2, 4525–4580, 2014

0.373 s and 0.385 s, respectively), but nevertheless we cannot clearly distinguish it from the overall variability.

Additional numerical experiments with fixed values of cohesion (1.25, 1.57 and 1.8 kPa) were made in order to determine the sensitivity of C_{FEM} results solely to values of angle of internal friction, ϕ (Table 3). For, example, the obtained values of C_{FEM9} (for $c = 1.57$ kPa, $\phi = 30$ or 40°) were equal to 0.365 and 0.477 s, respectively (Fig. 10). Compared to the value of 0.373 s (for the pair 1.57 kPa – 35°), it is obvious that the response of results to ϕ is negligible and therefore we are still unable to name a single optimal value of the friction angle. ~~Some further discussion of the obtained C_{FEM} profiles along ϕ (with c = constant) will follow in the subsequent Sect. 6.~~

Owing to the fact that for the search through the parameter space we used the "calibration" sample, we ran three "validation" sample simulations (tests: 25, 31, 37, 40, 42, 43) for verification of the parameters that were responsible for the lowest C_{FEM} (1.57 kPa – 30°, 1.57 kPa – 35° and 1.6 kPa – 30°). Excluding test 25, which presented an outlier for the three simulation sets, the "validation" samples produced similarly low C_{FEM} values to those that were made with the "calibration" sample (Table 3; $C_{FEM5} = 0.406$, 0.377 and 0.394 s, respectively). For example, for simulations with $c = 1.57$ kPa and $\phi = 35°$, the time difference between modeled and observed failures correspond, on average, to 5 % of the total duration of each individual test.

5.3 Sensitivity tests

In the following we briefly describe the sensitivity tests, which were performed in order to confirm that none of the results provided above are affected by other parameters of the model. These tests were performed during different stages of the model development and testing, therefore here we just summarize the main conclusions.

The ranges of values used for the sensitivity analysis are specified in Table 2. The most important point to highlight is that none of these parameters had effects comparable to the impact of the parameters of the failure criteria, c and ϕ.

NHESSD
2, 4525–4580, 2014

Sensitivity tests with a higher Young's modulus, E, of the block (2 or 3 times higher; in line with the discussion about E variation due to strain-rates in Sect. 4.2.5) have shown negligible increase in the magnitude of stresses within the joint (about 1–2 %), and negligible effects on time-to-failure (t_m). Numerical experiments (s6y; for 9 tests) with the same cohesion, c, and angle of internal friction ϕ as in the s6 simulations (Table 3), but with a Young's modulus twice as high as in the control simulation, produced similar C_{FEM9} (0.383 s compared to 0.373 s of the control simulations; see Fig. 10 with details also shown in Table 3). Similarly, a threefold increase of Young's modulus (s6yy; for 9 tests) also did not produce significantly different C_{FEM9} (0.380 s).

Our sensitivity calculations with respect to Poisson's ratio, υ, in the block showed that a selection of 0.23 instead of 0.04 produces slightly higher normal stresses within the joint (1.1 % at the largest), and thus may delay timing of total failure but for only one time step (Δt). The effect on normal stress echoes conclusions of Curtis and Smith (1974).

An increase of the viscosity of the block, υ, by two or four orders of magnitude (from 10^4 Pa s up to 10^6 or 10^8 Pa s) has a negligible effect on failure time. Similarly, a decrease of viscosity by two orders of magnitude (from 10^4 down to 10^2 Pa s) also has no effect on the discussed results. The baseline value of 10^4 Pa s was found to be optimal for the overall behavior of the model (by optimal we mean no artifacts like artificial high-frequency oscillations or lag of stresses behind displacements).

Finally, relatively low sensitivity of failure properties of the model to different combinations of stiffness K_s and K_n was found. For example, three sensitivity sets of simulations performed for all 19 tests with the same c = 1.6 kPa and ϕ = 45°, but varied stiffness values (between 10^3 and 10^8 N m^{-3}), produced very similar results in terms of the cost function. In other words, the difference in terms of failure time is not comparable with the magnitude produced by changes in cohesion, c, and angle of internal friction, ϕ.

NHESSD
2, 4525–4580, 2014

6 Discussion

The objective of the study was to investigate the applicability of the Mohr–Coulomb failure criterion, which is one of the most common criterions in mechanics of granular material (Sect. 3.3). ~~The previous section (5) has shown~~ that even with a simple set of model assumptions, it ~~could be~~ possible to reproduce very different cases (i.e. with various inclinations, masses and sizes) observed during relatively complex experiments. The fact that we find parameters of c and ϕ that also give low C_{FEM} for other tests provides another justification that the approach with the Mohr–Coulomb failure criterion, used in this study, is appropriate for modeling failure in the experiments. In our approach, as elsewhere, the criterion plays a role of a failure threshold. The fulfillment of the failure condition is a load-driven process due to stress inhomogeneity, which is caused by inertial and geometrical effects. Because of the latter, normal stress oscillations in particular impose a requirement of the interface to have tensile strength, σ_{st}, in addition to the cohesion, c. This means that the weak layer is dependent on the friction angle, and cannot be described by a purely cohesive form of the Mohr–Coulomb failure criterion.

To highlight the meaning of the cost function C_{FEM} results indicated in Fig. 10 in terms of the Mohr–Coulomb failure criterion, we plotted all numerical tests against the most "successful" simulations (i.e. those that have minimal C_{FEM}) in Fig. 11. On the Fig. 11 we have used green shading and red lines only for results in which the C_{FEM} is lower than 0.5 s (for both types of sample sizes, i.e. with 5 or 9 tests). Strong constraints for the value of cohesion are evident (1.6–1.8 kPa) (Fig. 11). The cohesion values obtained through our inverse simulations fall well within the range of measurements reported for weak layers composed from precipitation particles or interfaces (Föhn et al., 1998).

Additionally, for comparison, previous analytically derived experimental values (Podolskiy et al., 2010b) are plotted over the modeling results (Fig. 11). These analytical results indicated a dependence on normal load, and Fig. 11 clearly illustrates that normal stress oscillations and their variability between the tests make the analytical

NHESSD
2, 4525–4580, 2014

solution hard to interpret without FEM modeling. This also means that the normal stress dependence is an important ingredient of the model which should be accounted for.

As Fig. 11 shows, the global minima could not be clearly resolved for some particular pairs and thus the cost function is presented by a minima "valley" (Figs. 10 and 11). The latter corresponds to a narrow bottleneck of limited cohesion values, c. Thus modeling suggests that the overall behavior of the observed failures is mostly controlled by a value of cohesion, c (Fig. 11). For the same cohesion a variation of the angle of friction (within the range 20 to 60°) did not have significant effect on the reproduction of failures (as described in more details below). It is probable that the obtained minima "landscape" is due to a limited range of sample heights, inclinations and thus experimental normal stresses, which may be insufficient for further clarification of angle of internal friction, ϕ. Another explanation for the poorly localized minima may stem from a slight variability between tests.

Additional interpretation of the performance of the Mohr–Coulomb failure criterion, employed in this study, could be stated as follows (it corresponds to the classical graphical meaning of the criterion). For a fixed value of cohesion, c, which is considered as the shear strength at zero normal stress (where sign simply depends on a direction of shearing), the angle of internal friction, ϕ, corresponds to the slope of the envelope and controls, on one hand, the value of the tensile strength, σ_{st}, and on the other hand the linear "strengthening" of the interface with higher compression (e.g. Fig. 11). Meaning that, for example, with the angle of internal friction higher than 45°, tensile strength of the interface becomes smaller than the cohesion, and at the same time, the compressive part of the criterion steepens and requires higher shear stress for failure. On the contrary, a lower angle of internal friction (< 45°) increases the tensile strength of the interface compared to the cohesion, and at the same time gives a lower inclination of the envelope in compressive mode. Due to stress inhomogeneity caused by inertia, inclination and geometry, the above described dual effects are always superimposed onto each other in simulations. Thus, for an instance of high ϕ, if some edge nodes easily "failed" in tension at a given oscillation, the rest of nodes will be stronger in

NHESSD
2, 4525–4580, 2014

compression. Such dual effect due to mixed failure conditions in the interface highlights the importance of accounting for the angle of internal friction, and explains reasons for comparable time of model failure obtained for some tests computed with fixed cohesion, but different ϕ (e.g. Fig. 8; ~~tests: 23, 26, 30, 39, 40~~).

Nevertheless, if we assume 90° inclination of the platform, we may expect that the angle of internal friction will become a more important factor due to the higher tensile component of stress, and thus high angles of internal friction (i.e. $> 45°$) would correspond to higher values of the cost function. For tests with fixed cohesion (Fig. 12), this suggestion can be supported by C_{FEM} shown only for inclined tests (27, 33, 26, 32), which becomes smaller for 30–35° and increases for higher angles of internal friction (Fig. 12). Meaning that this range may be considered as the potential global minima.

Previous experimental data on the angle of internal friction is very scarce. However, it is worthwhile to note that by plotting the homogeneous snow tensile strength, σ_{st}, against the shear strength one may identify the inclination of the Mohr–Coulomb failure envelope for snow (and thus obtain the failure ϕ). For this we attempt to plot experimental measurements (from 14 different studies assembled by Gaume, 2012) of the two against snow density in Fig. 13a (for more tensile measurements see Borstad, 2011). If we try to deduce values of the angle of friction, as $\arctan(\tau_{\mathrm{st}}/\sigma_{\mathrm{st}})$, by assuming exponential fits for shear and tension strengths for all available data (Fig. 13b), such values will remain approximately within a range of 10 to 40° (Fig. 13c), meaning that the tensile strength is higher than the shear strength. This is in agreement with Roch (1966) and Mellor (1975), however, since natural variation of strength measurements is high, the considered data includes various types of snow, and exponential fits have low R^2 (power fits yielded similar values), the conclusions remain to be verified. By comparing results of the modeling (Fig. 12) with the literature (Figs. 13 and 14), there is overall consistency with most of the considered data sources, including those in Fig. 14b.

Nevertheless, previously published values of ϕ vary strongly depending on the literature source (Fig. 14a and b). Approximately thirty degrees is commonly used (Schweizer et al., 2004; Gaume et al., 2012). But the value may range from 5.7 to 57.7°

NHESSD
2, 4525–4580, 2014

in experimental data (Keeler and Weeks, 1968; Mellor, 1975; McClung and Schaerer, 2006) (for example, van Herwijnen and Heierli, 2009 measured the residual friction angle in the field and obtained a result of about 30°), or deviate to 45° for avalanche fracture line analyses (Jamieson et al., 2001), or even to 73.4 and 83.1° for shaking platform tests (Nakamura et al., 2010). Thus, this clearly indicates that the question still remains open to further clarification and distinction between different types of friction angles. Nevertheless, keeping in mind the previous remark, if we consider a combination of the above mentioned observation on the ratio between the shear and tensile strength (Figs. 13 and 14) and our numerically obtained results (Fig. 12), we could suggest that the value around 30–35° may be the most physically realistic value for snow that is similar in terms of its type and density.

Finally, we note that the linear shape of the Mohr–Coulomb failure envelope, which is responsible for the effects mentioned above, was just assumed in this study. Furthermore, the likely limitation of our approach is a non-obvious projection of the results onto the domain of higher compressions, in particular due to size effects. Such interesting questions and refinement of the law by other effects (as discussed in Sect. 3.3) remain open for future work, which for instance, could consider a closure of the envelope for compression, as well as incorporate other shapes of the envelope; see e.g. Haefeli (1963).

The simple model used here provides a reasonable match to the experiments. In the present form our results may not be applicable for failure in a plane perpendicular to weak layers when no shear is applied, and we do not make any claim that the model is universal in relation to fracture propagation. Accordingly the presented constitutive behaviour should be used only for predicting the sample scale shear stress at which snow is expected to fail in a brittle manner.

NHESSD
2, 4525–4580, 2014

7 Conclusions

This paper presents a FEM study to simulate snow weak layer failure under cyclic acceleration loading and to analyze the performance of the Mohr–Coulomb failure criterion. The model is tested by comparison with previous cold-laboratory results for shaking platform experiments (Podolskiy et al., 2010b). An ensemble of individual experiments is simulated and analyzed for overall sensitivity to the adjustment of the constitutive parameters. Based on more than 500 simulations, we found that the linear elasticity of snow blocks and the Mohr–Coulomb failure criterion for the interface with zero thickness representing the weak layer are sufficient and adequate for snow failure analysis of the experiments. Best-fit couples of cohesion and angle of internal friction, c and ϕ, were found to be [1.6 kPa, 22.5–60°]. The wide range of ϕ highlights the fact that the reproduction of experiments is largely controlled by an absolute value of cohesion and has relatively low sensitivity to the angle of internal friction (within the limit shown above). Basing on values of the cost function for a limited sample of inclined tests (Fig. 12) and on previous experimental evidence (Fig. 13), we could suggest that ϕ around 30–35° is the most optimal value, which may be further clarified with follow-up studies. Nevertheless, the requirements to consider effects of normal stress on failure, and to include the tensile strength of the interface were evident, meaning that a purely cohesive form of the Mohr–Coulomb failure criterion is not applicable. The tensile strength could be limited to a range between 0.9 and 3.8 kPa (Table 3), which is comparable to previously reported results (see Fig. 13a).

The FE results are compared with the previously used analytical solution (Nakamura et al., 2010; Podolskiy et al., 2010b), which was found to be inadequate for estimating shear stresses along the failure plane for cases with any inclination of the platform. Shear stresses produced during the inclined tests (25 or 35°) were found to be highly non-homogeneous and thus poorly represented by the analytical approach. Accordingly, the interpretation of experiments through the previously used analytical (or "static") solution is limited, due to substantial edge effects (originating from non-uniform

NHESSD
2, 4525–4580, 2014

normal stress oscillations from compression into tension and caused by interplay between inertial and geometrical effects).

Finally, we are aware that our model with the weak layer representation employed here is only one of many possible approaches, which could have been used to fit the data, and that we confronted the method against only one type of weak layer (composed from precipitation particles) used in previous experiments. Nevertheless, the reasonable results, described in this paper, suggest that our approach may be further verified and developed (for instance, for non-linear shapes of the failure criterion) and may be also applied to other types of loadings and weak layers. Such work along with computationally expensive comparison against other failure criteria could constitute follow-up studies.

One of conclusions by Stoffel (2005) was that the application of the Finite Element Method would never be possible in daily avalanche forecasting due to unknown spatial and temporal variation of weak layer properties and uncertainty with the weather. Nevertheless, as our study shows, mechanical application of the method may provide powerful tools for analysis, extraction and validation of theoretical or empirical laws from experimental data for their further usage. Hence, validation of the model and the formulation of an explicit cost function for the optimization of the model create a platform and open perspectives for interpretation of experiments and follow-up theoretical studies and analysis. For example, after solving a challenging scientific question of size-effect re-scaling, the obtained values (in combination with other parameters) could be used at larger scales for modeling slope releases or in studies aimed at the impact of seismic loading on snow-covered slopes (Podolskiy et al., 2010a).

Acknowledgements. The research leading to these results has received funding from International Affairs Directorate of IRSTEA, INTERREG ALCOTRA (MAP3), from the People Programme (Marie Curie Actions) of the European Union's Seventh Framework Programme (FP7/2007-2013) under REA grant agreement #298672 (FP7-PEOPLE-2011-IIF, "TRIME"), and from LabEx OSUG@2020 (Investissements d'avenir – ANR10 LABX56). EAP is grateful for all the support, also to E. A. Hardwick, N. Hadda, P. Hagenmuller, T. Faug and M. Schneebeli

NHESSD
2, 4525–4580, 2014

for help and for comments on initial version of the manuscript. The quality of the paper was improved thanks to remarks by the two anonymous reviewers.

References

Abe, O. and Nakamura, T.: A new method of measurements of the shear strength of snow, horizontal vibration method, Snow Life Tohoku, 15, 13–14, 2000. 4531

Abe, O. and Nakamura, T.: Shear fracture strength of snow measured by the horizontal vibration method, J. Snow Eng., 21, 11–12, 2005. 4531

Bader, H. and Salm, B.: On the mechanics of snow slab release, Cold Reg. Sci. Technol., 17, 287–300, 1990. 4527, 4528

Baroudi, D., Sovilla, B., and Thibert, E.: Effects of flow regime and sensor geometry on snow avalanche impact-pressure measurements, J. Glaciol., 57, 277–288, doi:10.3189/002214311796405988, 2011. 4529

Bazant, Z. P., Zi, G., and McClung, D.: Size effect law and fracture mechanics of the triggering of dry snow slab avalanches, J. Geophys. Res., 108, doi:10.1029/2002JB001884, 2003. 4527, 4537

Birkeland, K., Schweizer, J., and Jamieson, B.: Fracture propagation: recent research and implications, Avalanche Rev., 27, 287–300, 2009. 4530, 4534

Borstad, C. P.: Tensile strength and fracture of cohesive dry snow related to slab avalanches, Ph.D. thesis, University of British Columbia, Vancouver, Canada, 2011. 4553

Borstad, C. P. and McClung, D.: Numerical modeling of tensile fracture initiation and propagation in snow slabs using nonlocal damage mechanics, Cold Reg. Sci. Technol., 69, 145–155, doi:10.1016/j.coldregions.2011.09.010, 2011. 4537, 4542

Chiaia, B. and Frigo, B.: A scale-invariant model for snow slab avalanches, J. Stat. Mech., 2009, P02056, doi:10.1088/1742-5468/2009/02/P02056, 2009. 4526

Chiaia, B., Cornetti, P., and Frigo, B.: Triggering of dry snow slab avalanches: stress vs. fracture mechanical approach, Cold Reg. Sci. Technol., 53, 170–178, doi:10.1016/j.coldregions.2007.08.003, 2008. 4527, 4529

Curtis, J. O. and Smith, F. W.: Material property and boundary condition effects on stresses in avalanche snow-packs, J. Glaciol., 13, 99–108, 1974 4527, 4550

NHESSD

2, 4525–4580, 2014

DeMontmollin, V.: Introduction a la rheologie de la neige, Ph.D. thesis, Universite Scientifique et Medicale de Grenoble, France, 1978. 4534

DeMontmollin, V.: Shear tests on snow explained by fast metamorphism, J. Glaciol., 28, 187–198, 1982. 4534

Fierz, C., Armstrong, R. L., Durand, Y., Etchevers, P., Greene, E., McClung, D. M., Nishimura, K., Satayawali, P. K., and Sokratov, S. A.: The international classification for seasonal snow on the ground, IHP-VII Technical Documents in Hydrology #83, IACS Contribution #1, Tech. rep., UNESCO – International Hydrological Programme, Paris, 2009. 4532

Föhn, P., Camponovo, C., and Krüsi, G.: Mechanical and structural properties of weak snow layers measured in situ, Ann. Glaciol., 26, 1–6, 1998. 4528, 4544, 4551

Fyffe, B. and Zaiser, M.: The effects of snow variability on slab avalanche release, Cold Reg. Sci. Technol., 40, 229–242, doi:10.1016/j.coldregions.2004.08.004, 2004. 4526

Gaume, J.: Evaluation of avalanche release depths. Combined statistical – mechanical modeling, Ph. D. thesis, IRSTEA/Universite de Grenoble, St.-Martin-d'Hères, France, 2012. 4527, 4536, 4553, 4579

Gaume, J., Chambon, G., Naaim, M., and Eckert, N.: Influence of Weak Layer Heterogeneity on Slab Avalanche Release Using a Finite Element Method, in: Advances in Bifurcation and Degradation in Geomaterials, edited by: Bonelli, S., Dascalu, C., and Nicot, F., vol. 11 of Springer Series in Geomechanics and Geoengineering, Springer Netherlands, 261–266, doi:10.1007/978-94-007-1421-2_34, 2011. 4527, 4536

Gaume, J., Chambon, G., Eckert, N., and Naaim, M.: Relative influence of mechanical and meteorological factors on avalanche release depth distributions: an application to French Alps, Geophys. Res. Lett., 39, L12401, doi:10.1029/2012GL051917, 2012. 4527, 4528, 4536, 4553

Gaume, J., Chambon, G., Eckert, N., and Naaim, M.: Influence of weak-layer heterogeneity on snow slab avalanche release: application to the evaluation of avalanche release depths, J. Glaciol., 59, 423–437, doi:10.3189/2013JoG12J161, 2013. 4527, 4536

Gubler, H.: Physik von Schnee, Skriptum, Tech. rep., Eidgenössisches Institut für Schnee- und Lawinenforschung, Davos, 1994. 4542

Habermann, M., Schweizer, J., and Jamieson, J. B.: Influence of snowpack layering on human-triggered snow slab avalanche release, Cold Reg. Sci. Technol., 54, 176–182, doi:10.1016/j.coldregions.2008.05.003, 2008. 4527, 4541, 4542

NHESSD

2, 4525–4580, 2014

Haefeli, R.: Stress transformations, tensile strengths, and rupture processes of the snow cover, in: Ice and Snow: Properties, Processes, and Applications, edited by: Kingery, W., M.I.T. Press, Cambridge, Mass., 560–575, 1963. 4534, 4554
Heierli, J., Gumbsch, P., and Zaiser, M.: Anticrack nucleation as triggering mechanism for snow slab avalanches, Science, 321, 240–243, doi:10.1126/science.1153948, 2008. 4527, 4530, 4537
Jamieson, B. and Johnston, C. D.: Evaluation of the shear frame test for weak snowpack layers, Ann. Glaciol., 32, 59–69, doi:10.3189/172756401781819472, 2001. 4527, 4528, 4541, 4542
Jamieson, B., Geldsetzer, T., and Stethem, C.: Forecasting for deep slab avalanches, Cold Reg. Sci. Technol., 33, 275–290, doi:10.1016/S0165-232X(01)00056-8, 2001. 4554
Jamieson, J. B. and Johnston, C. D.: Refinements to the stability index for skier-triggered dry-slab avalanches, Ann. Glaciol., 26, 296–302, 1998. 4534
Jamieson, J. B. and Schweizer, J.: Texture and strength changes of buried surface-hoar layers with implications for dry snow-slab avalanche release, J. Glaciol., 46, 151–160, doi:10.3189/172756500781833278, 2000. 4542
Jones, A., Jamieson, J., and Schweizer, J.: The effect of slab and bed surface stiffness on the skier-induced shear stress in weak snowpack layers, Proceedings of International Snow Science Workshop (ISSW-2006), 157–164, 2006. 4527
Keeler, C. M. and Weeks, W. F.: Investigations into the mechanical properties of alpine snow-packs, J. Glaciol., 7, 253–271, 1968. 4544, 4554
Kry, P. R.: The relationship between the visco-elastic and structural properties of fine-grained snow, J. Glaciol., 14, 479–500, 1968. 4541
Laborderie, C. and Jeanvoine, E.: Beginning with Castem 2000, Tech. Rep. DMT/94-356, CEA, Saclay, France, 1994. 4536
Lang, T. and Sommerfeld, R.: The modeling and measurement of the deformation of a sloping snow-pack, J. Glaciol., 19, 153–163, 1977. 4527
Louge, M. Y., Carroll, C. S., and Turnbull, B.: Role of pore pressure gradients in sustaining frontal particle entrainment in eruption currents: The case of powder snow avalanches, J. Geophys. Res., 116, F04030, doi:10.1029/2011JF002065, 2011. 4529, 4534
Mahajan, P. and Joshi, S.: Modeling of interfacial crack velocities in snow, Cold Reg. Sci. Technol., 51, 98–111, doi:10.1016/j.coldregions.2007.05.008, 2008. 4527, 4528, 4543

NHESSD
2, 4525–4580, 2014

Mahajan, P. and Senthil, S.: Cohesive element modeling of crack growth in a layered snowpack, Cold Reg. Sci. Technol., 40, 111–122, doi:10.1016/j.coldregions.2004.06.006, 2004. 4527, 4528, 4543

Mahajan, P., Kalakuntla, R., and Chandel, C.: Numerical simulation of failure in a layered thin snowpack under skier load, Ann. Glaciol., 51, 169–175, doi:10.3189/172756410791386436, 2010. 4527, 4528, 4537

Matsushita, H., Matsuzawa, M., and Abe, O.: The influences of temperature and normal load on the shear strength of snow consisting of precipitation particles, Ann. Glaciol., 53, 31–38, doi:10.3189/2012AoG61A022, 2012. 4534, 4535

Matsushita, H., Ikeda, S., Ito, Y., Matsuzawa, M., and Nakamura, H.: Avalanches induced by earthquake in North Tochigi prefecture on 25 February 2013, in: Proceedings of International Snow Science Workshop, ISSW'13, Grenoble-Chamonix, France, 1122–1129, 2013. 4529

McClung, D. M.: Direct simple shear tests on snow and their relation to slab avalanche formation, J. Glaciol., 19, 101–109, 1977. 4534

McClung, D. M.: Shear fracture precipitated by strain softening as a mechanism of dry slab avalanche release, J. Geophys. Res., 84, 3519–3526, doi:10.1029/JB084iB07p03519, 1979. 4526, 4527, 4528, 4542

McClung, D. M.: Analysis of critical length measurements for dry snow slab weak-layer shear fracture, J. Glaciol., 57, 557–566, doi:10.3189/002214311796905541, 2011a. 4534, 4542

McClung, D. M.: The critical size of macroscopic imperfections in dry snow slab avalanche initiation, J. Geophys. Res., 116, F03003, doi:10.1029/2010JF001866, 2011b. 4530

McClung, D. M. and Borstad, C. P.: Deformation and energy of dry snow slabs prior to fracture propagation, J. Glaciol., 58, 553–564, doi:10.3189/2012JoG11J009, 2012. 4534

McClung, D. M. and Schaerer, P.: The Avalanche Handbook, 3rd Edn., The Mountaineers Books, Seattle, Wash, 2006. 4528, 4535, 4554

Mellor, M.: A review of basic snow mechanics, in: Publ. 114, Int. Assoc. of Hydrol. Sci., Geneva, Switzerland, 251–291, 1975. 4534, 4541, 4542, 4553, 4554, 4564, 4579

Miller, D., Tichota, R., and Adams, E.: An explicit numerical model for the study of snow's response to explosive air blast, Cold Reg. Sci. Technol., 69, 156–164, doi:10.1016/j.coldregions.2011.08.004, 2011. 4527, 4528

Naaim, M., Faug, T., and Naaim-Bouvet, F.: Dry granular flow modelling including erosion and deposition, Surv. Geophys., 24, 569–585, doi:10.1023/B:GEOP.0000006083.47240.4c, 2003. 4527

NHESSD

2, 4525–4580, 2014

Nakamura, T., Abe, O., Nohguchi, M., and Kobayashi, T.: Basic studies on the behavior of roof snow in vibration in a snow season at earthquakes, Snow Life Tohoku, 15, 19–22, 2000a. 4531

Nakamura, T., Hashimoto, R., Abe, O., and Ohta, T.: Experience with shear frames, Snow Life Tohoku, 15, 15–18, 2000b. 4531

Nakamura, T., Abe, O., Hashimoto, R., and Ohta, T.: A dynamic method to measure the shear strength of snow, J. Glaciol., 56, 333–338, doi:10.3189/002214310791968502, 2010. 4531, 4532, 4535, 4540, 4541, 4544, 4554, 4555

Nakamura, T., Abe, O., Hashimoto, R., and Ohta, T.: Correction: a dynamic method to measure the shear strength of snow, J. Glaciol., 58, 818, 2012. 4541

Nakaya, U.: Elastic properties of processed snow with reference to its internal structure, Research Report 82, Tech. rep., US Army Cold Regions Research and Engineering Lab., Hanover, NH, USA, 1961. 4541

Navarre, J. P., Taillefer, A., and Danielou, Y.: Fluage et rhéologie de la neige, Actes de Conférence Chamonix, 14–25 Septembre 1992, Chamonix, 377–388, 1992. 4534

Ooizumi, M. and Huzioka, T.: Studies of the behavior of a snow cover on a mountain slope, II. Poisson's ratio of snow, Low Temp. Sci. Ser. A, 41, 43–53, 1982. 4542

Pérez-Guillén, C., Tapia, M., Suriñach, E., Furdada, G., and Hiller, M.: Evaluation of an avalanche triggered by a local earthquake at the Vallée de la Sionne (Switzerland) experimental site, in: Proceedings of International Snow Science Workshop, ISSW'13, Grenoble-Chamonix, France, 183–190, 2013. 4529

Perla, R. and Beck, T. M. H.: Experience with shear frames, J. Glaciol., 29, 485–491, 1983. 4534

Podolskiy, E. A., Nishimura, K., Abe, O., and Chernous, P. A.: Earthquake-induced snow avalanches: I. Historical case studies, J. Glaciol., 56, 431–446, doi:10.3189/002214310792447815, 2010a. 4528, 4534, 4556

Podolskiy, E. A., Nishimura, K., Abe, O., and Chernous, P. A.: Earthquake-induced snow avalanches: II. Experimental study, J. Glaciol., 56, 447–458, doi:10.3189/002214310792447833, 2010b. 4529, 4530, 4531, 4532, 4533, 4535, 4536, 4540, 4551, 4555, 4564, 4577

Podolskiy, E. A., Chambon, G., Naaim, M., and Gaume, J.: A review of finite element modelling in snow mechanics, J. Glaciol., 59, 1189–1201, doi:10.3189/2013JoG13J121, 2013. 4526, 4527, 4536, 4541

NHESSD
2, 4525–4580, 2014

Reiweger, I. and Schweizer, J.: Failure of a layer of buried surface hoar, Geophys. Res. Lett., 37, L24501, doi:10.1029/2010GL045433, 2010. 4530, 4534
Reiweger, I., Schweizer, J., Dual, J., and Herrmann, H. J.: Modelling snow failure with a ibre bundle model, J. Glaciol., 55, 997–1002, doi:10.3189/002214309790794869, 2009. 4526
Roch, A.: Les variations de la résistance de la neige, in: International Association of Scientific Hydrology Publication 69, Symposium at Davos, 5–10 April 1965, Scientific Aspects of Snow and Ice Avalanches, Davos, 86–99, 1966. 4534, 4553
Salm, B.: On the rheological behavior of snow under high stresses, Contrib. Inst. Low Temp. Sci. Ser. A, 23, 1–43, 1971. 4542
Schweizer, J.: The influence of the layered character of snow cover on the triggering of slab avalanches, Ann. Glaciol., 18, 193–198, 1993. 4527
Schweizer, J.: Review of dry snow slab avalanche release, Cold Reg. Sci. Technol., 30, 43–57, doi:10.1016/S0165-232X(99)00025-7, 1999. 4542
Schweizer, J., Michot, G., and Kirchner, H.: On the fracture toughness of snow, Ann. Glaciol., 38, 1–8, doi:10.3189/172756404781814906, 2004. 4553
Shapiro, L., Johnson, J., Sturm, M., and Blaisdell, G.: Snow mechanics – review of the state of knowledge and applications, Research Report 97-3, Tech. rep., US Army Cold Regions Research and Engineering Lab., Hanover, NH, USA, 1997. 4541
Sigrist, C. and Schweizer, J.: Critical energy release rates of weak snowpack layers determined in field experiments, Geophys. Res. Lett., 34, L03502, doi:10.1029/2006GL028576, 2007. 4527
Sigrist, C., Schweizer, J., Schindler, H.-J., and Dual, J.: The energy release rate of mode II fractures in layered snow samples, Internat. J. Fract., 139, 461–475, doi:10.1007/s10704-006-6580-9, 2006. 4527, 4543
Smith, F. and Curtis, J.: Stress analysis and failure prediction in avalanche snowpacks, in: Publ. 114, Int. Assoc. of Hydrol. Sci., Geneva, Switzerland, 332–340, 1975. 4527
Smith, F., Sommerfeld, R. A., and Bailey, R. O.: Finite-element stress analysis of avalanche snowpacks, J. Glaciol., 10, 401–405, 1972. 4527
Stoffel, M.: Numerical modelling of snow using finite elements, Ph.D. thesis, Swiss Fed. Inst. of Technol., Zürich, Switzerland, 2005. 4526, 4527, 4541, 4556
Stoffel, M. and Bartelt, P.: Modelling snow slab release using a temperature-dependent viscoelastic Finite Element model with weak layers, Surv. Geophys., 24, 417–430, doi:10.1023/B:GEOP.0000006074.56474.43, 2003. 4527, 4528

NHESSD
2, 4525–4580, 2014

Teufelsbauer, H.: Linking laser scanning to snowpack modeling: data processing and visualization, Comput. Geosci., 35, 1481–1490, doi:10.1016/j.cageo.2008.10.006, 2009. 4527
Teufelsbauer, H.: A two-dimensional snow creep model for alpine terrain, Nat. Hazards, 56, 481–497, doi:10.1007/s11069-010-9515-8, 2011. 4527, 4542
van Herwijnen, A. and Birkeland, K.: Measurements of snow slab displacement in extended column tests and comparison with propagation saw tests, Cold Reg. Sci. Technol., 97, 97–103, doi:10.1016/j.coldregions.2013.07.002, 2014. 4535
van Herwijnen, A. and Heierli, J.: Measurement of crack-face friction in collapsed weak snow layers, Geophys. Res. Lett., 36, L23502, doi:10.1029/2009GL040389, 2009. 4554
van Herwijnen, A. and Jamieson, B.: High-speed photography of fractures in weak snowpack layers, Cold Reg. Sci. Technol., 43, 71–82, 2005. 4533
van Herwijnen, A., Schweizer, J., and Heierli, J.: Measurement of the deformation field associated with fracture propagation in weak snowpack layers, J. Geophys. Res., 115, F03042, doi:10.1029/2009JF001515, 2010. 4533
Vidal, L.: Modelisation de la rupture d'une plaque de neige et mode de fonctionnement d'une couche fragile, Ph.D. thesis, Universite Joseph Fourier, Grenoble, France, 2001. 4534
Wilson, A., Schweizer, J., Johnston, C., and Jamieson, J.: Effects of surface warming of adry snowpack, Cold Reg. Sci. Technol., 30, 59–65, doi:10.1016/S0165-232X(99)00014-2, 1999. 4527
Zeidler, A. and Jamieson, B.: Refinements of empirical models to forecast the shear strength of persistent weak layers, Part A: Layers of faceted crystals., Cold Reg. Sci. Technol., 44, 194–205, 2006. 4526

NHESSD
2, 4525–4580, 2014

Table 1. List of tests referred for validation of the model, after Podolskiy et al. (2010b) and prescribed modeling parameters for each test.

#	Platform inclination (°)	Mass of fractured snow, m_f (kg)	Peak horizontal acceleration a_p (g)	Total time of vibration until fracture (s)	Estimated shear strength, τ_{ex} (kPa)	Estimated normal pressure at failure, σ (kPa)	Mean density of the block, (kg m^{-3})	Frequency coefficient, k_ω s^{-2}	h_s – equivalent for FE model (m)	Young's modulus of block (MPa) as function of density, after (Mellor, 1975)
17	0	2.06	5.56	18.6	1.97	−0.35	226	0.44	0.15	1.5
20	0	2.25	5.72	14.2	2.13	−0.37	226	0.57	0.16	1.5
23	0	2.02	4.96	9.6	1.66	−0.33	226	0.74	0.14	1.5
25	0	2.18	6.36	9.8	2.34	−0.37	218	0.82	0.16	1.3
30	0	2.11	5.05	8.0	1.65	−0.32	218	0.86	0.14	1.3
31	0	2.12	5.33	5.7	1.85	−0.35	218	1.14	0.15	1.3
35	0	2.42	5.91	5.4	2.37	−0.40	212	1.24	0.18	1.2
42	0	2.29	5.55	4.2	2.15	−0.39	212	1.43	0.18	1.2
43	0	2.40	4.41	4.3	1.72	−0.39	212	1.26	0.18	1.2
37	0	3.50	3.51	4.7	1.97	−0.56	212	1.06	0.26	1.2
39	0	4.60	2.70	2.8	2.06	−0.76	212	1.28	0.36	1.2
40	0	4.54	2.80	3.2	2.11	−0.76	212	1.21	0.35	1.2
41	0	4.03	2.63	2.9	1.76	−0.67	212	1.24	0.31	1.2
19	35	1.34	2.23	7.2	0.52	0.10	226	0.62	0.10	1.5
26	35	2.20	3.52	4.8	1.29	0.45	218	1.04	0.17	1.3
27	35	2.22	3.62	8.6	1.28	0.46	218	0.68	0.17	1.3
24	25	1.98	2.53	6.8	0.85	0.05	226	0.69	0.15	1.5
32	25	1.92	4.47	8.7	1.13	0.87	218	0.75	0.15	1.3
33	25	2.04	4.26	8.4	1.15	0.90	218	0.76	0.16	1.3

NHESSD
2, 4525–4580, 2014

Table 2. Properties of FEM model (values in square brackets correspond to sensitivity tests).

Object	Property	Value
Block	Length, l	0.3 m
	Height, h_s	0.10–0.36 m
	Density, ρ	212–226 kg m^{-3}
	Young's modulus, E	1.2×10^6–1.5×10^6 Pa [×2 or ×3]
	Poisson's ratio, υ	0.04 [0.23]
	Viscosity, η	10^4 Pa s [10^2–10^8 Pa s]
Interface	Length, l	0.3 m
	Shear stiffness, K_s	1×10^8 N m^{-3} [10^5–10^8 N m^{-3}]
	Normal stiffness, K_n	1×10^8 N m^{-3} [10^5–10^8 N m^{-3}]
	Cohesion, c	[0.5–2.5 kPa, 2.8 kPa]
	Angle of friction, ϕ	[10–75°]
Boundary	Inclination	0°, 25°, 35°
	Oscillations (max amplitude)	Horizontal (16.5 mm)

NHESSD
2, 4525–4580, 2014

Table 3. Sample response to adjustment parameters (see also Fig. 10)[1].

Run code name	ϕ, °	σ_{st}, Pa	c, Pa	C_{FEM5} for 5 tests (27, 30, 33, 35, 41)	C_{FEM9} for 9 tests (27, 30, 33, 35, 41, 23, 26, 32, 39)	C_{FEM6} for 6 validation tests (25, 31, 37, 40, 42, 43)/C_{FEM5} for 5 validation tests (same without 25)
s1	55	750	1071.1	1.569	–	–
s2	55	1250	1785.2	0.504	0.570	–
s3	45	1000	1000.0	1.746	–	–
s4	45	2000	2000.0	0.875	–	–
s5	35	1250	875.3	2.154	–	–
s6	35	2250	1575.5	0.465	0.373	0.749/0.377
phi	30	2728.8	1575.5	0.463	0.365	0.821/0.406
phi1	40	1877.6	1575.5	0.532	0.477	–
phi2	25	3378.6	1575.5	0.519	0.424	–
s6y[1]	35	2250	1575.5	0.476	0.383	–
s6yy[2]	35	2250	1575.5	0.476	0.380	–
s7	35	3000	2100.6	1.576	–	–
s8	60	500	866.0	2.072	–	–
c3&8	45	1600	1600.0	0.506	0.434	–
c4&9	30	1600	923.8	2.131	–	–
c5&10	60	1600	2771.3	1.722	–	–
c6&11	30	2771.3	1600.0	0.496	0.385	0.794/0.394
c7&12	60	923.7	1600.0	0.454	0.448	–
s9	15	5879.7	1575.5	0.645	0.559	–
s10	75	422.154	1575.5	1.873	1.771	–
s11	22.5	3803.6	1575.5	0.539	0.443	–
s12	67.5	652.6	1575.5	1.017	0.940	–
s15[3]	35	2250	1575.5	0.483	0.404	–
s14[4]	35	2250	1575.5	0.478	0.412	–
s16[5]	35	2250	1575.5	0.446	0.362	–
phi3	50	1322.0	1575.5	0.499	0.513	–
phi4	60	909.6	1575.5	0.501	0.518	–
phi5	30	2684.7	1550	0.476	0.363	–
phi6	20	3434.3	1250	1.047	0.976	–
phi7	30	2165.1	1250	1.033	0.949	–
phi8	40	1489.7	1250	1.049	0.946	–
phi9	50	1048.9	1250	1.096	0.992	–
phi10	60	721.7	1250	1.153	1.118	–
phi11	20	4945.5	1800	0.909	0.869	–
phi12	30	3117.7	1800	0.738	0.744	–
phi13	40	2145.2	1800	0.740	0.723	–
phi14	50	1510.4	1800	0.723	0.750	–
phi15	60	1039.2	1800	0.441	0.485	0.416/0.411
phi16	60	1154.7	2000	0.762	0.810	–
phi17	67.5	517.77	1250	1.428	1.384	–
phi18	67.5	745.58	1800	0.808	0.786	–
phi19	67.5	828.43	2000	0.738	0.776	–
phi20	15	4665.1	1250	1.070	0.997	–
phi21	15	6717.7	1800	0.996	0.964	–
phi22	15	7464.1	2000	1.418	1.399	–
phi23	10	8935.1	1575.5	0.746	0.665	–
phi24	60	1212.8	2100	0.950	0.886	–
phi25	75	482.314	1800	1.565	1.462	–
phi26	75	562.67	2100	1.200	1.150	–
phi27	57.5	1075.2	1687.8	0.467	0.510	–

[1] Sensitivity tests to higher E, ×2; [2] Sensitivity tests to higher E, ×3; [3] Sensitivity tests to higher η, $\times 10^2$; [4] Sensitivity tests to higher η, $\times 10^4$; [5] Sensitivity tests to lower η, $\times 10^{-2}$

NHESSD
2, 4525–4580, 2014

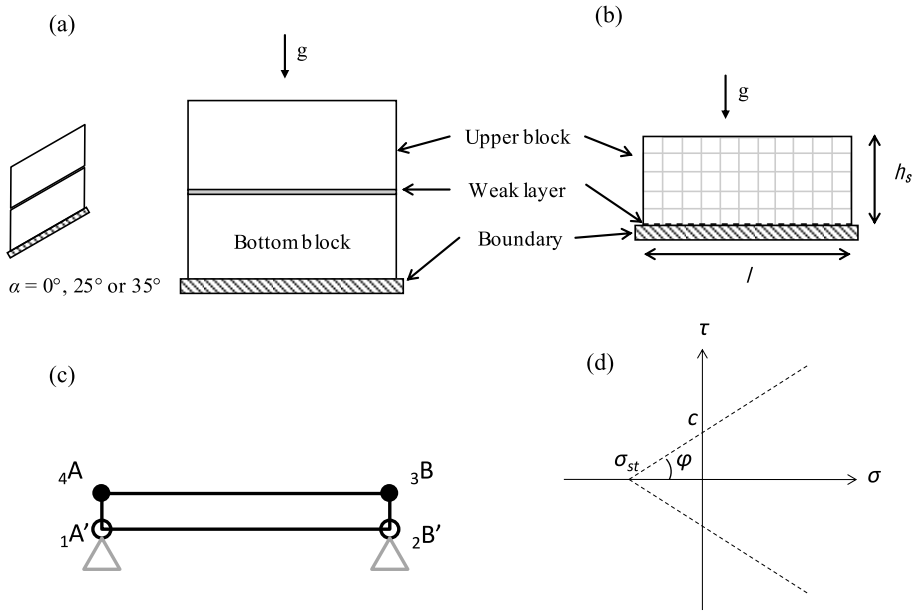

Figure 1. (a) 2-D geometry of the discussed experiments and **(b)** an example of corresponding geometry in Finite Element model; **(c)** schematic of the joint element; **(d)** Mohr–Coulomb failure criterion.

NHESSD
2, 4525–4580, 2014

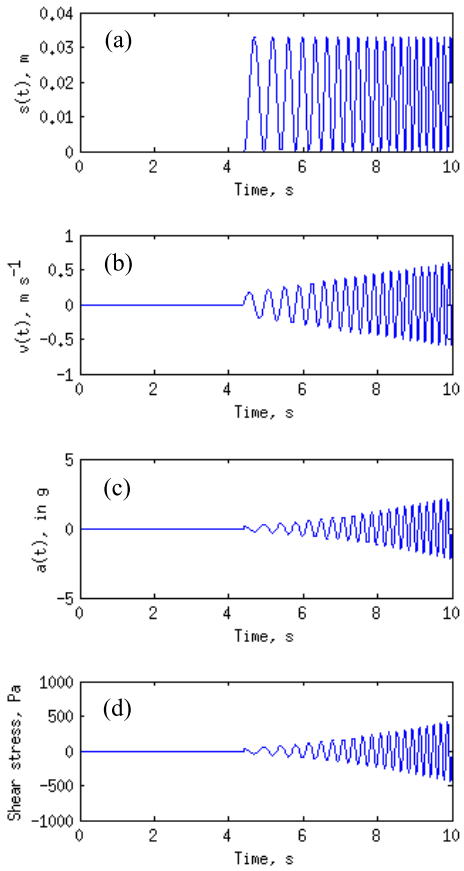

Figure 2. Examples of imposed displacements, $s(t)$, its derivatives and analytical estimation of shear stress. **(a)** Imposed displacements, $s(t)$ (k_ω=0.74 s^{-2}); **(b)** velocity, $s'(t)$; **(c)** acceleration, $s''(t)$; **(d)** analytical shear stress, τ_a (for h_s = 0.1 m, ρ = 200 kg m^{-3}).

NHESSD
2, 4525–4580, 2014

Evaluating snow weak-layer rupture parameters

E. A. Podolskiy et al.

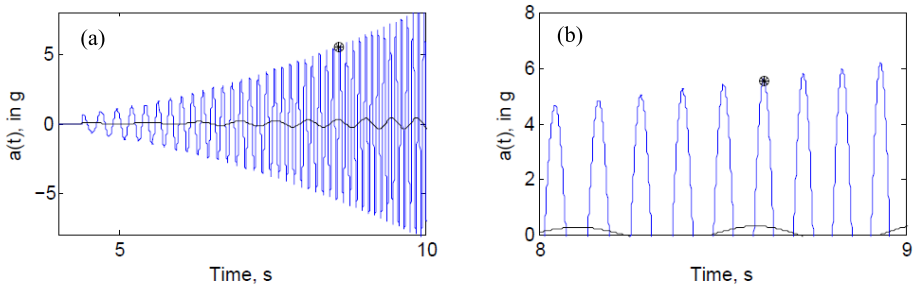

Figure 3. Examples of fitting angular frequency by adjusting k_ω: **(a)** $k_\omega = 0.33\,s^{-2}$ (in black) and $1.43\,s^{-2}$ (in blue), **(b)** same zoomed; Markers indicate an example of observed peak acceleration reached at observed failure time.

NHESSD
2, 4525–4580, 2014

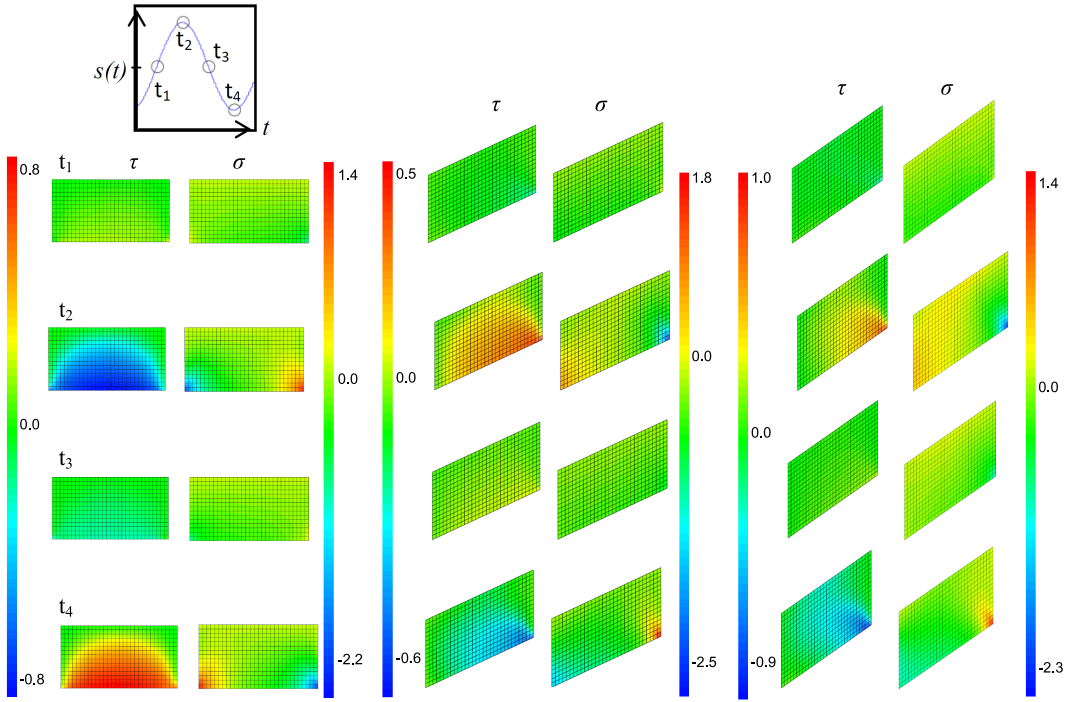

Figure 4. Shear and normal stress concentrations within blocks (inclined to 0, 25 or 35°) at different consequent phases of oscillations (time increases downward; the inset of the figure shows an example of corresponding instants on the trajectory, i.e. time–displacement plane). (For each inclination left side corresponds to shear, τ, right side – to normal pressure, σ. Note that color intensity is not normalized in order to highlight specific concentrations for each case; in 10^3 Pa).

NHESSD
2, 4525–4580, 2014

Evaluating snow weak-layer rupture parameters

E. A. Podolskiy et al.

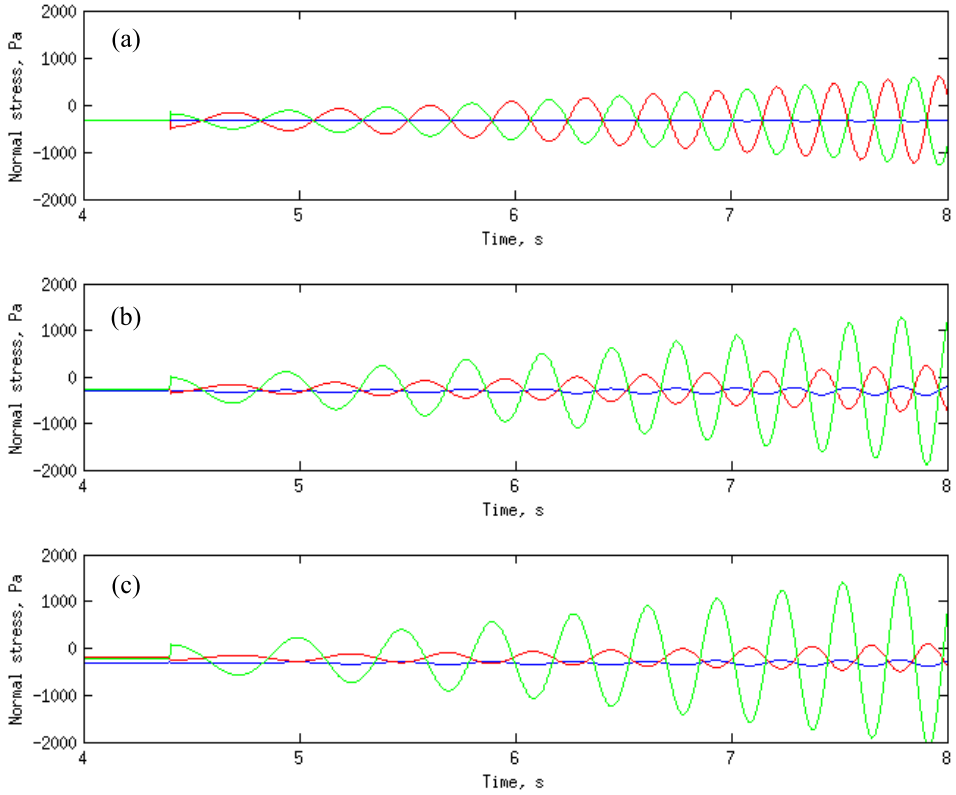

Figure 5. Example of evolution of normal stresses in the middle and at edges of the interface (blue corresponds to the middle of the interface; red – to the lower edge; green – to the upper edge). **(a)** horizontal test (Test 23); **(b)** and **(c)** – inclined tests (25 and 35°; Tests 33 and 27).

NHESSD
2, 4525–4580, 2014

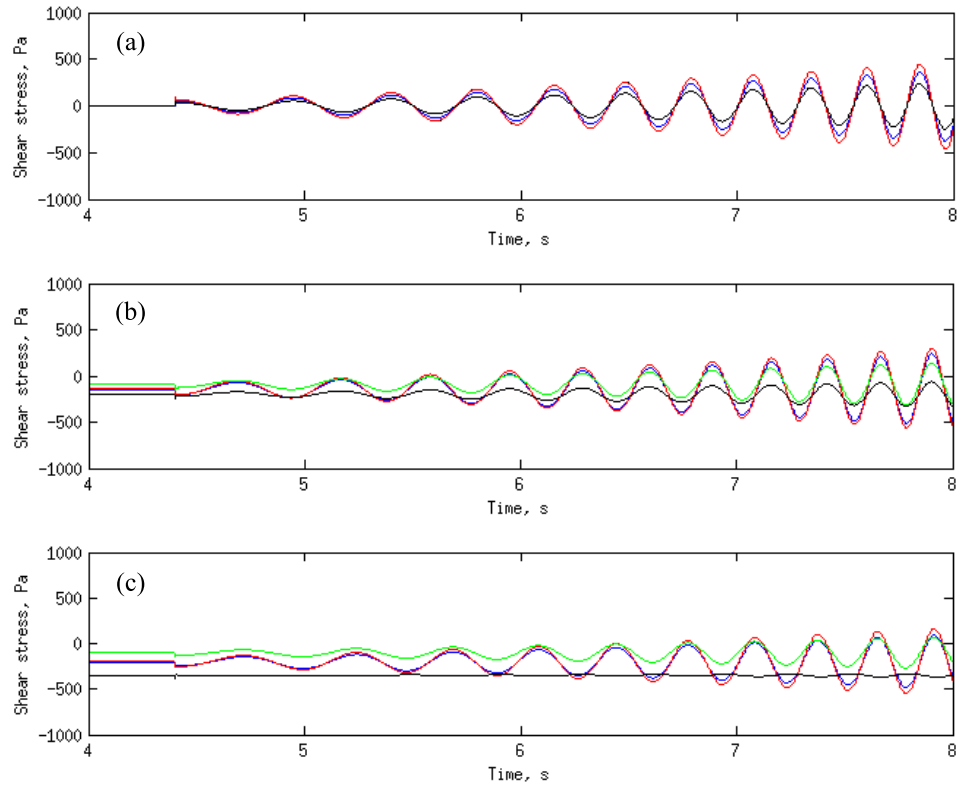

Figure 6. Examples showing shear stress differences between simple analytical and FEM solutions. **(a)** horizontal test, 0° (Test 23, $h = 0.14$ m, $\rho = 226\,\mathrm{kg\,m^{-3}}$); **(b)** inclined test, 25° (Test 33: $h = 0.16$ m, $\rho = 218\,\mathrm{kg\,m^{-3}}$); **(c)** inclined test, 35° (Test 27: $h = 0.17$ m, $\rho = 218\,\mathrm{kg\,m^{-3}}$). Analytical solutions are shown in blue; FEM – in red (for the middle of the joint), green (left or upper edge), and black (right or lower edge).

NHESSD
2, 4525–4580, 2014

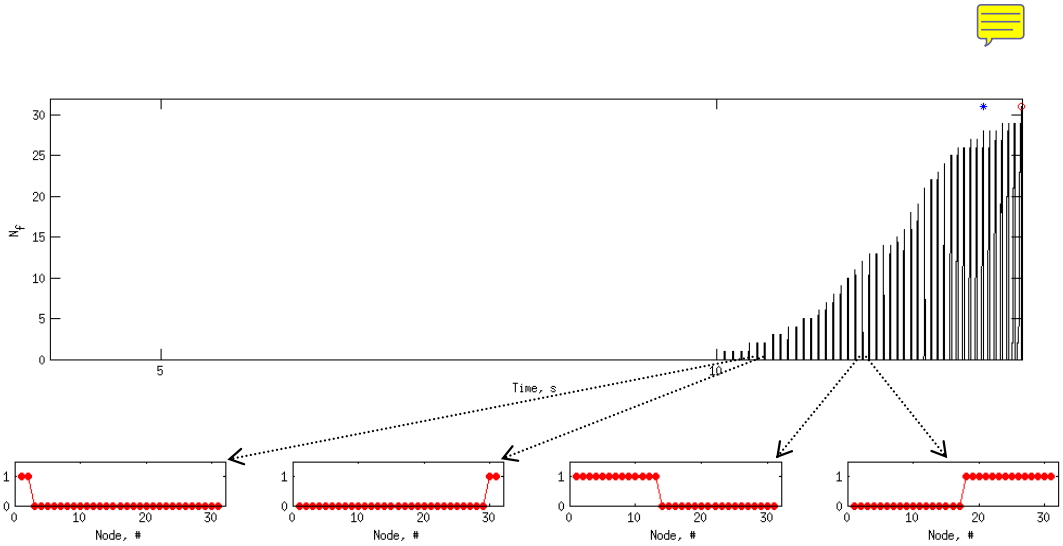

Figure 7. Example of N_f growth with simulation time (for test 30: c = 1.6 kPa, ϕ = 30°, ($t_m - t_e$) = 0.3 s): i.e. instantaneous number of nodes under failure criterion, N_f (t_e is shown by a blue asterisk, t_m by a red circle). Illustrations below indicate which nodes along the length of the interface satisfy failure criterion (i.e. yes – "1", no – "0") at particular instants.

NHESSD
2, 4525–4580, 2014

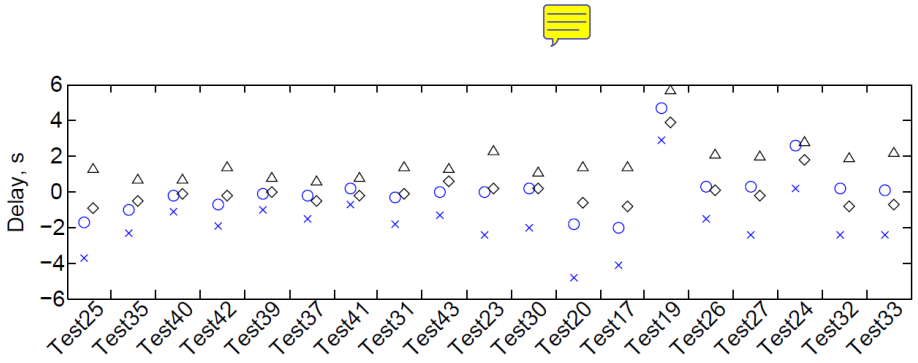

Figure 8. Example of delays between observed and modeled failures ($t_m - t_e$) for different tests as a function of adjustment parameters (ϕ, c). Blue circles correspond to 30°–1.6 kPa, blue crosses to 30°–0.9 kPa; black triangles to 30°–2.7 kPa, black diamonds to 60°–1.6 kPa.

NHESSD
2, 4525–4580, 2014

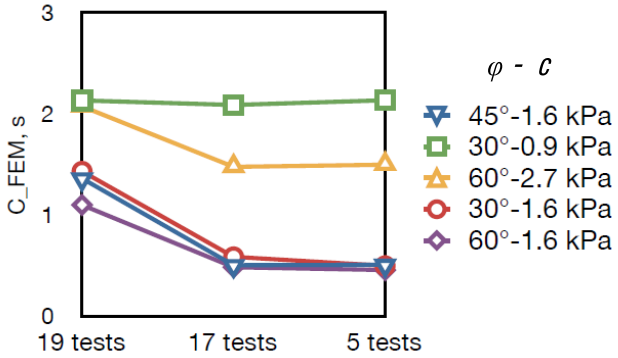

Figure 9. Comparison between C_{FEM} obtained for (1) whole population of tests with stiffness K_s and $K_n = 10^8$ N m^{-3} (C_{FEM19}; 19 tests), (2) for a population excluding outliers and computationally expensive tests (C_{FEM15}; 15 tests: i.e. without 17, 19, 20, 24), and (3) for a sample of the population (C_{FEM5}; 5 tests: only 27, 30, 33, 35, 41).

NHESSD
2, 4525–4580, 2014

Evaluating snow weak-layer rupture parameters

E. A. Podolskiy et al.

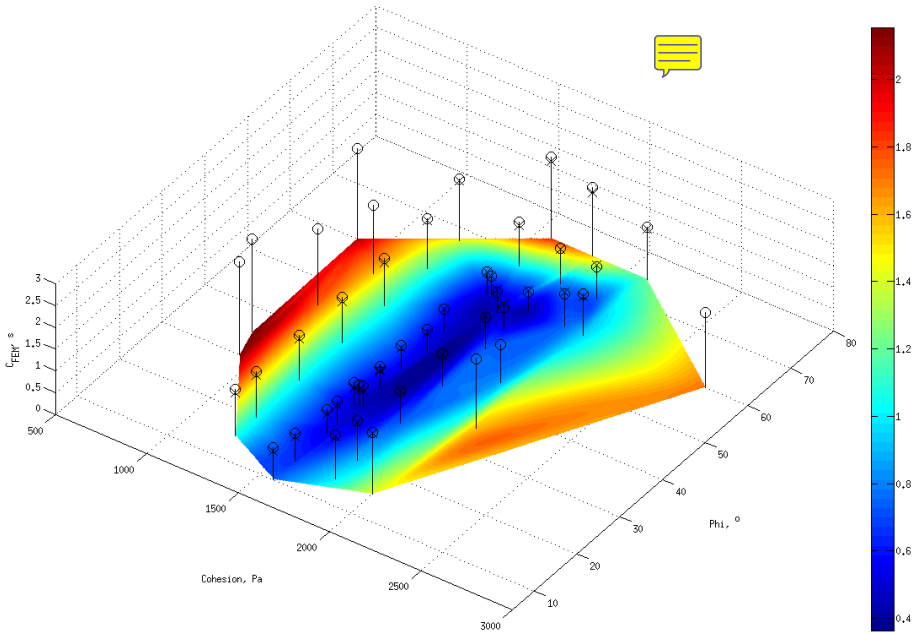

Figure 10. Effects of c and ϕ adjustments on time delay between modeled and experimental failures (C_{FEM}, or RMSE; shown for a sample of 5 tests by empty circles, for a sample of 9 tests by crosses, and for Young's modulus sensitivity tests, s6y and s6yy, by pentagrams). Color contours are based on cubic interpolation for generalization of results (C_{FEM5}).

NHESSD
2, 4525–4580, 2014

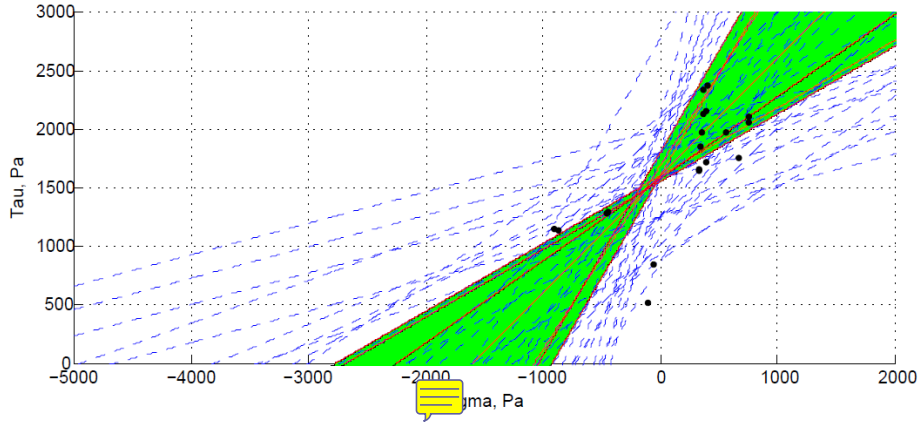

Figure 11. Illustration of all tested pairs of c and ϕ as parameters of the Mohr–Coulomb failure criterion (blue dashed lines); red curves (with green shading) indicate the most successful simulations (i.e. when both C_{FEM}, for the representative sample of 5 or 9 tests, are ≤ 0.5 s). Circles indicate previous analytically derived experimental results (Podolskiy et al., 2010b).

NHESSD
2, 4525–4580, 2014

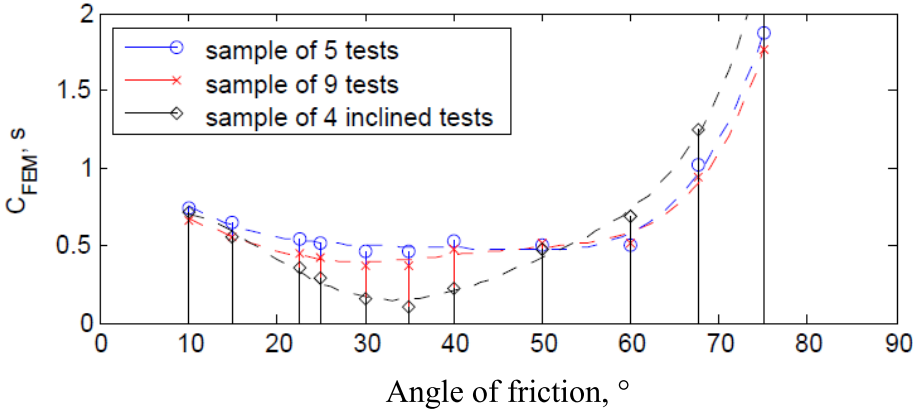

Figure 12. Effect of the angle of friction, ϕ, on C_{FEM} for simulations with the same cohesion 1.57 kPa (shown for a sample of 5 tests by blue empty circles, for a sample of 9 tests by red crosses, for a sample of 4 inclined tests by black diamonds).

NHESSD
2, 4525–4580, 2014

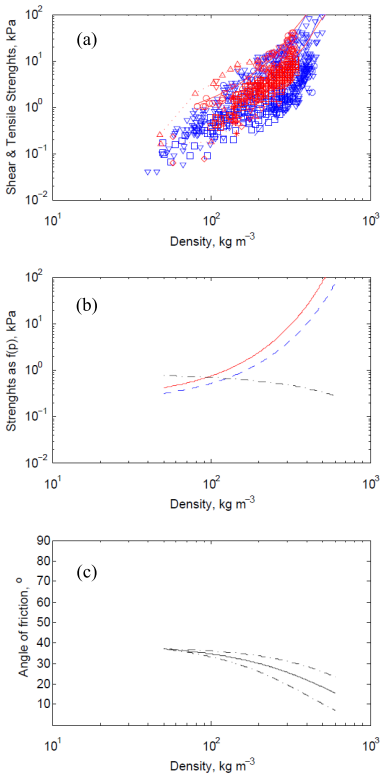

Figure 13. (a) Experimental measurements of snow shear (in blue) and tensile (in red) strengths as functions of density from multiple studies and for different snow types; curves refer to (Mellor, 1975); for details and full bibliographic references see (Gaume, 2012); **(b)** Exponential fits for shear and tensile strengths ($0.191e^{0.0099\rho}$, $R^2 = 0.57$, and $0.231e^{0.0117\rho}$, R^2=0.62, respectively); dash-dot curve shows shear fit divided by tension fit ($0.8251e^{-0.0018\rho}$). **(c)** Corresponding arctangent of the shear to tension proportion; dash-dot curves indicate the boundaries of the absolute propagated uncertainty (which is $|\Delta f(x_i)| = \sum_{i=1}^{n} |\frac{\partial f}{\partial x_i}||\Delta x_i|$).

NHESSD
2, 4525–4580, 2014

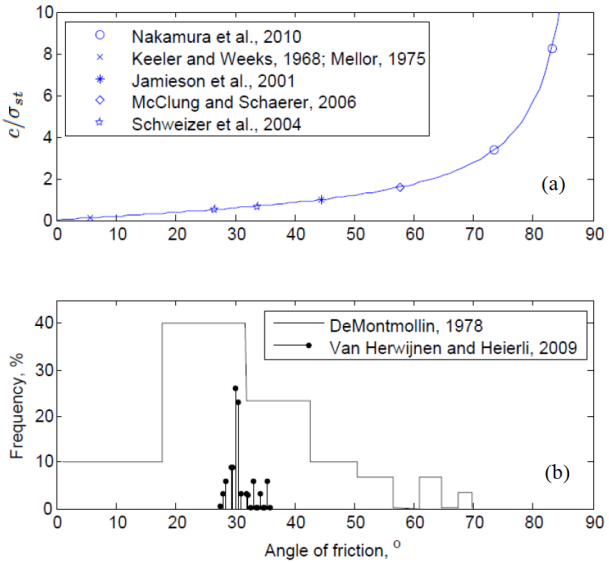

Figure 14. (a), **(b)** Examples of values of the angle of friction obtained from different studies (y axis in **a** corresponds to $\tan\phi$, which is equal to c/σ_{st} and shown as a blue curve). It is plotted this way in order to visualize the ratio between cohesion and tensile strength).

NHESSD
2, 4525–4580, 2014